Advances in Water Resources 62 (2013) 254–265

Contents lists available at ScienceDirect

Advances in Water Resources

journal homepage: www.elsevier.com/locate/advwatres

Homogenizability conditions for multicomponent reactive transport

Francesca Boso [a], Ilenia Battiato [b,*]

[a] Department of Mechanical and Aerospace Engineering, University of California, San Diego, 9500 Gilman Dr., La Jolla, CA 92093, USA
[b] Department of Mechanical Engineering, Clemson University, Clemson, SC 29634, USA

ARTICLE INFO

Article history:
Available online 9 August 2013

Keywords:
Upscaling
Homogeneous reaction
Heterogeneous reaction
Multicomponent reactive transport
Dissolution
Precipitation

ABSTRACT

We consider multicomponent reactive transport in porous media involving three reacting species, two of which undergo a nonlinear homogeneous reaction, while a third precipitates on the solid matrix through a heterogeneous nonlinear reaction. The process is fully reversible and can be described with a reaction of the kind $A + B \rightleftharpoons C \rightleftharpoons S$. The system's behavior is fully controlled by Péclet (Pe) and three Damköhler (Da_j, $j = \{1, 2, 3\}$) numbers, which quantify the relative importance of the four key mechanisms involved in the transport process, i.e. advection, molecular diffusion, homogeneous and heterogeneous reactions. We use multiple-scale expansions to upscale the pore-scale system of equations to the macroscale, and establish sufficient conditions under which macroscopic local advection–dispersion–reaction equations (ADREs) provide an accurate representation of the pore-scale processes. These conditions reveal that (i) the heterogeneous reaction leads to more stringent constraints compared to the homogeneous reactions, and (ii) advection can favorably enhance pore-scale mixing in the presence of fast reactions and relatively low molecular diffusion. Such conditions are summarized by a phase diagram in the (Pe,Da_j)-space, and verified through numerical simulations of multicomponent transport in a planar fracture with reacting walls. Our computations suggest that the constraints derived in our analysis are robust in identifying sufficient as well as necessary conditions for homogenizability.

1. Introduction

Nonlinear reactive transport in media with micro-structure is ubiquitous to many environmental, industrial and biological systems. While a majority of classical results in porous media theory have been obtained in the context of single- and multi-phase subsurface transport [8,13,19], more effective recent investigations have focused on biological systems, e.g. calcium dynamics in cell membranes [12,18], and technological applications [4]. Other applications include chemical weathering, contaminant transport in aquifers [8], and geologic CO_2 sequestration [27].

The plethora of scales involved in such systems allows one to employ two general approaches in modeling transport phenomena: pore-scale or Darcy-scale (macroscopic, upscaled, continuum) models. Pore-scale simulations, e.g. pore-network models, lattice Boltzmann simulations [33], and particle methods [29], are based on first principles, and therefore have strong physical foundations. Such models allow one to gain significant insight in the physical process at the pore-scale. However, they require the knowledge of pore-scale geometry at any location in the computational domain, information seldom available in most applications. This renders them impractical as a predictive tool at spatial and temporal scales much larger than the pore-scale. Continuum-scale models are based on an effective medium representation of the system with effective transport parameters such as porosity, dispersion coefficient, hydraulic conductivity, and effective reaction rates. Since upscaled models significantly alleviate computational burden, they are routinely used to model reaction processes at the macro-scale. However they rely on phenomenological descriptions and/or closure assumptions which typically include geometrical constraints that guarantee scale separation between the pore- and continuum-scales, linearization of pore-scale equations, and empirical closures, just to mention a few. These assumptions are often necessary to fully decouple the pore-scale description and its continuum counterpart, and to obtain a local upscaled equation. Upscaling techniques - e.g. volume averaging [36], the methods of moments [11], homogenization [19] and its modifications to include evolving microstructure [1,28], pore-network models, and thermodynamically constrained averaging [16] – allow one to formally establish the connection between pore- and continuum-scale models.

While Darcy's law has proven to be very robust in modeling flow through porous media from the field- (i.e. kilometer-) to the micron-scale [3,4], the advection–dispersion-reaction equations (ADREs) fail to capture a number of observed transport features, including the extent of reactions in mixing-controlled chemical transformations [38] and asymmetrical long tails of breakthrough

* Corresponding author.
E-mail address: ibattia@clemson.edu (I. Battiato).

0309-1708/$ - see front matter © 2013 Elsevier Ltd. All rights reserved.
http://dx.doi.org/10.1016/j.advwatres.2013.07.014

curves [26], just to mention a few. Further, scale dependence of effective transport parameters [21,22] and discrepancy between lab and field experiments have long been recognized. They are attributed to concentration gradients and mass transport limitations at the pore-scale [24]. These shortcomings manifest themselves when the approximations and/or closure assumptions underlying the continuum model are not fulfilled. Most upscaling studies focus on the derivation of effective medium representations for specific physical and geochemical processes [15, and references therein]. However, they rarely specify in which range of parameters or physical regimes (e.g. diffusion- or reaction-controlled), such continuum-scale models are valid. Therefore, the application of macroscopic models to reactive systems with strong chemical/physical heterogeneity can be problematic since pore-scale reaction rates might exhibit a broad variability, and the transport process span significantly different regimes [38, and references therein].

The growing attention towards the mathematical foundations of effective models and the connection between pore-scale processes and their representation at the continuum scale is reflected by the increasing interest in modeling reactive transport at the micro-scale [9,29,33,37], and the concurrent development of multi-algorithm (or hybrid) models which combine descriptions at different scales [7,31,33]. In a number of works, e.g. [24,32], pore-scale simulations served as a tool to both gain insight in the physical processes, and to verify the validity of macroscopic models. Fewer are the works which have explicitly addressed the problem of establishing conditions under which the pore-scale processes correctly upscale to local macroscopic equations, e.g. [2,5,6,23,35]. Studies on the applicability range of macroscopic equations have involved the advection–dispersion equation (ADE) for conservative transport [2], the Taylor dispersion problem in a fracture with reactive walls [23], purely reactive–diffusive multicomponent systems with nonlinear homogeneous reactions [6], and single component advective systems with nonlinear heterogeneous reactions [5]. The influence of mixing on the effective reaction rate has had a long history in mathematics and engineering, e.g. [14,38, and references therein].

In this work we generalize [5] by considering multicomponent reactive transport in porous media involving three reacting species, two of which undergo a nonlinear homogeneous reaction in the liquid phase, while a third precipitates on the solid matrix through a heterogeneous nonlinear reaction at the solid–liquid interface. The fully reversible biomolecular precipitation/dissolution process can be described with a reaction of the type $A + B \rightleftharpoons C \rightleftharpoons S$. Calcite precipitation provides one example for this type of reactions [24]. Additionally, numerical simulations of multi-component reactive flow in a planar fracture are employed to verify the homogenizability conditions derived by multiple-scale expansions.

We start, in Section 2, by formulating a pore-scale model for the system under consideration, and by defining the dimensionless Péclet (Pe) and three Damköhler ($\mathrm{Da}_j,\ j = \{1,2,3\}$) numbers which quantify the relative importance of the four key mechanisms involved in the transport process, i.e. advection, molecular diffusion, homogeneous and heterogeneous reactions. In Section 3, by means of multiple-scale expansions [19], we upscale the pore-scale system of equations to the macroscale, and establish sufficient conditions under which macroscopic local advection–dispersion–reaction equations (ADREs) provide an accurate representation of pore-scale processes. Such conditions are summarized by a phase diagram in the (Pe,Da_j)-space. Section 4 discusses a number of special cases. In Section 5 we verify the previously derived conditions through pore-scale numerical simulations of multicomponent transport in a planar fracture with reacting walls. Finally, the main results are summarized in the concluding Section 6.

2. Problem formulation

Consider reactive transport in a porous medium $\hat{\Omega}$ whose characteristic length is L. Let us assume that the medium can be represented microscopically by a collection of spatially periodic "unit cells" $\hat{Y}$ with a characteristic length ℓ, and a scale parameter $\varepsilon \equiv \ell/L \ll 1$. The unit cell $\hat{Y} = \hat{\mathcal{B}} \cup \hat{\mathcal{G}}$ consists of the pore space $\hat{\mathcal{B}}$ and the impermeable solid matrix $\hat{\mathcal{G}}$, separated by the smooth surface $\hat{\Gamma}$. The pore spaces $\hat{\mathcal{B}}$ of each cell $\hat{Y}$ form a multi-connected pore-space domain $\hat{\mathcal{B}}^\varepsilon \subset \hat{\Omega}$ bounded by the smooth surface $\hat{\Gamma}^\varepsilon$.

2.1. Governing equations

Let us assume the porous medium to be fully saturated with an incompressible fluid. Single-phase incompressible Stokes flow in the pore-space $\hat{\mathcal{B}}^\varepsilon$ is described by the Stokes and continuity equations subject to the no-slip boundary condition on $\hat{\Gamma}^\varepsilon$,

$$\nu\hat{\nabla}^2\hat{\mathbf{v}}_\varepsilon - \hat{\nabla}\hat{p} = 0, \quad \hat{\nabla}\cdot\hat{\mathbf{v}}_\varepsilon = 0, \quad \hat{\mathbf{x}} \in \hat{\mathcal{B}}^\varepsilon, \quad \hat{\mathbf{v}}_\varepsilon = \mathbf{0}, \quad \hat{\mathbf{x}} \in \hat{\Gamma}^\varepsilon, \tag{1}$$

where $\hat{\mathbf{v}}_\varepsilon(\hat{\mathbf{x}})$ is the fluid velocity, $\hat{p}$ denotes the fluid dynamic pressure, and ν is the dynamic viscosity. The liquid is a solution of two chemical (or biological) species A and B (with concentrations $\hat{a}_\varepsilon(\hat{\mathbf{x}},\hat{t})$ and $\hat{b}_\varepsilon(\hat{\mathbf{x}},\hat{t})$ at point $\hat{\mathbf{x}} \in \hat{\mathcal{B}}^\varepsilon$ and time $\hat{t}$, respectively) that react to form an aqueous reaction product C. Whenever $\hat{c}_\varepsilon(\hat{\mathbf{x}},\hat{t})$, the concentration of C, exceeds a threshold value $\overline{c}$ in proximity of a reactive wall, C undergoes a heterogeneous reaction and precipitates on the solid matrix, forming a precipitate S. In general, this process is fully reversible, and its speed is controlled by the reaction rates k_{ab}, k, k_c and k_d corresponding to the following reactions,

$$A + B \overset{k_{ab}}{\rightarrow} C \overset{k}{\rightarrow} S \quad \text{and} \quad A + B \overset{k_c}{\leftarrow} C \overset{k_d}{\leftarrow} S. \tag{2}$$

The aqueous concentrations $\hat{a}_\varepsilon(\hat{\mathbf{x}},\hat{t}), \hat{b}_\varepsilon(\hat{\mathbf{x}},\hat{t})$ and $\hat{c}_\varepsilon(\hat{\mathbf{x}},\hat{t})$ [mol L^{-3} satisfy a system of advection–reaction–diffusion equations (ARDEs)

$$\partial_{\hat{t}}\hat{a}_\varepsilon = \hat{\nabla}\cdot(\mathcal{D}_a\hat{\nabla}\hat{a}_\varepsilon - \hat{\mathbf{v}}_\varepsilon\hat{a}_\varepsilon) - k_{ab}\hat{a}_\varepsilon\hat{b}_\varepsilon + k_c\hat{c}_\varepsilon, \quad \hat{\mathbf{x}} \in \hat{\mathcal{B}}^\varepsilon,\ \hat{t} > 0 \tag{3a}$$

$$\partial_{\hat{t}}\hat{b}_\varepsilon = \hat{\nabla}\cdot(\mathcal{D}_b\hat{\nabla}\hat{b}_\varepsilon - \hat{\mathbf{v}}_\varepsilon\hat{b}_\varepsilon) - k_{ab}\hat{a}_\varepsilon\hat{b}_\varepsilon + k_c\hat{c}_\varepsilon, \quad \hat{\mathbf{x}} \in \hat{\mathcal{B}}^\varepsilon,\ \hat{t} > 0 \tag{3b}$$

$$\partial_{\hat{t}}\hat{c}_\varepsilon = \hat{\nabla}\cdot(\mathcal{D}_c\hat{\nabla}\hat{c}_\varepsilon - \hat{\mathbf{v}}_\varepsilon\hat{c}_\varepsilon) + k_{ab}\hat{a}_\varepsilon\hat{b}_\varepsilon - k_c\hat{c}_\varepsilon, \quad \hat{\mathbf{x}} \in \hat{\mathcal{B}}^\varepsilon,\ \hat{t} > 0, \tag{3c}$$

where the molecular diffusion coefficient $\mathcal{D}_i$, $i = \{a,b,c\}$, is, in general, a positive-definite second-rank tensor. At the solid–liquid interface $\hat{\Gamma}^\varepsilon$ impermeable to flow, mass flux of the species C is balanced by the difference between the precipitation and dissolution rates, $R_p = k\hat{c}_\varepsilon^n$ and $R_d = k_d$, respectively [20]. Therefore,

$$-\mathbf{n}\cdot\mathcal{D}_c\hat{\nabla}\hat{c}_\varepsilon = k(\hat{c}_\varepsilon^n - \overline{c}^n), \quad \hat{\mathbf{x}} \in \hat{\Gamma}^\varepsilon,\ \hat{t} > 0, \tag{4}$$

where $\mathbf{n}$ is the outward unit normal vector of $\hat{\Gamma}^\varepsilon$, k $[L^{3n-2}T^{-1}mol^{1-n}]$ is the heterogeneous reaction rate constant, $n \in \mathbb{Z}^+$ is related to the order of reaction [25, Eq. 6] and the threshold concentration $\overline{c}^n = k_d/k$ represents the solubility product [25]. Due to precipitation on the solid–liquid interface, $\hat{\Gamma}^\varepsilon(\hat{t})$ evolves in time with velocity $\hat{\mathbf{v}}_s$, according to $\rho_s\hat{\mathbf{v}}_s\cdot\mathbf{n} = k(\hat{c}_\varepsilon^n - \overline{c}^n)$, where ρ_s is the molar density of the precipitate [34]. In the following analysis, we disregard precipitation-induced changes in pore geometry which occur on a time scale longer than the processes under investigation [6]. No-flux boundary conditions hold for species A and B on the (multi-connected) liquid–solid interface $\hat{\Gamma}^\varepsilon$, i.e.

$$\mathbf{n}\cdot(\mathcal{D}_a\hat{\nabla}\hat{a}_\varepsilon) = \mathbf{n}\cdot(\mathcal{D}_b\hat{\nabla}\hat{b}_\varepsilon) = 0. \tag{5}$$

Further, the flow and transport equations (1) and (3) are supplemented with proper boundary conditions on the external boundary of the flow domain $\hat{\Omega}$ and with the initial conditions

$$\hat{a}_\varepsilon(\hat{\mathbf{x}},0) = \hat{a}_{\mathrm{in}}(\hat{\mathbf{x}}), \quad \hat{b}_\varepsilon(\hat{\mathbf{x}},0) = \hat{b}_{\mathrm{in}}(\hat{\mathbf{x}}), \quad \hat{c}_\varepsilon(\hat{\mathbf{x}},0) = \hat{c}_{\mathrm{in}}(\hat{\mathbf{x}}). \tag{6}$$

Specifically, we consider a scenario in which reactants A and B, with initial concentrations $\hat{a}_{\text{in}} > 0$ and $\hat{b}_{\text{in}} > 0$ respectively, are initially (i.e. $\hat{t} < 0$) separated in space, and brought in contact with each other at time $\hat{t} = 0$. Therefore the initial concentration of reaction product C is $\hat{c}_{\text{in}} = 0$. Such initial distribution of the three species has the advantage of amplifying the reactions occurring along the reactive walls since $\hat{c}_{\text{in}} \neq \bar{c}$, and inducing the formation of a localized reacting front.

2.2. Dimensionless formulation

For the sake of simplicity, we assume that the three reacting species A, B and C have the same diffusion coefficient, i.e. $\mathcal{D}_a = \mathcal{D}_b = \mathcal{D}_c = \mathcal{D}$. We introduce the following dimensionless quantities

$$a_\varepsilon = \frac{\hat{a}_\varepsilon}{\hat{c}^\star}, \quad b_\varepsilon = \frac{\hat{b}_\varepsilon}{\hat{c}^\star}, \quad c_\varepsilon = \frac{\hat{c}_\varepsilon}{\bar{c}}, \quad \mathbf{D} = \frac{\mathcal{D}}{\mathcal{D}_0}, \quad \mathbf{x} = \frac{\hat{\mathbf{x}}}{L}, \quad \mathbf{v}_\varepsilon = \frac{\hat{\mathbf{v}}_\varepsilon}{U},$$
$$p = \frac{\hat{p}\ell^2}{\nu UL}, \tag{7}$$

where $U, \mathcal{D}_0$ and $\hat{c}^\star = \max\{\hat{a}_{\text{in}}, \hat{b}_{\text{in}}\}$ are characteristic values of $\hat{\mathbf{v}}_\varepsilon, \mathcal{D}$ and the concentration of the reactants A and B, respectively. Proper rescaling of pressure $\hat{p}$ ensures that the pressure gradient has the same order of magnitude of the viscous term, as prescribed by Stokes equation [2, Eqs. 15, 16]. Furthermore, the following time scales can be defined

$$\hat{t}_{\text{d}} = \frac{L^2}{\mathcal{D}_0}, \quad \hat{t}_{\text{a}} = \frac{L}{U}, \quad \hat{t}_{\text{r1}} = \frac{L}{k\bar{c}^{n-1}}, \quad \hat{t}_{\text{r2}} = \frac{1}{k_{ab}\hat{c}^\star}, \quad \hat{t}_{\text{r3}} = \frac{1}{k_c}, \tag{8}$$

where $\hat{t}_{\text{d}}$ and $\hat{t}_{\text{a}}$ are the time scales associated to diffusion and advection. The three reactions, i.e. heterogeneous, nonlinear homogeneous and linear homogeneous reactions, are described by the time scales $\hat{t}_{\text{r1}}, \hat{t}_{\text{r2}}$ and $\hat{t}_{\text{r3}}$, respectively. Ratios between these time scales define the dimensionless Péclet ($\hat{t}_{\text{d}}/\hat{t}_{\text{a}}$) and Damköhler ($\hat{t}_{\text{d}}/\hat{t}_{\text{rj}}$, $j = \{1,2,3\}$) numbers,

$$\text{Pe} = \frac{UL}{\mathcal{D}_0}, \quad \text{Da}_1 = \frac{Lk}{\mathcal{D}_0}\bar{c}^{n-1}, \quad \text{Da}_2 = \frac{L^2 k_{ab}}{\mathcal{D}_0}\hat{c}^\star, \quad \text{Da}_3 = \frac{L^2 k_c}{\mathcal{D}_0} \tag{9}$$

Rewriting (1), (2) and (3) in terms of the dimensionless quantities (7) and the dimensionless time $t = \hat{t}/\hat{t}_{\text{d}}$ yields a dimensionless form of the flow equations

$$\varepsilon^2\nabla^2\mathbf{v}_\varepsilon - \nabla p = 0, \quad \nabla\cdot\mathbf{v}_\varepsilon = 0, \quad \mathbf{x}\in\mathcal{B}^\varepsilon, \tag{10}$$

subject to

$$\mathbf{v}_\varepsilon = \mathbf{0}, \quad \mathbf{x}\in\Gamma^\varepsilon \tag{11}$$

and of the transport equations

$$\partial_t a_\varepsilon + \nabla\cdot(-\mathbf{D}\nabla a_\varepsilon + \text{Pe}\mathbf{v}_\varepsilon a_\varepsilon) = -\text{Da}_2 a_\varepsilon b_\varepsilon + \eta\text{Da}_3 c_\varepsilon, \tag{12a}$$
$$\partial_t b_\varepsilon + \nabla\cdot(-\mathbf{D}\nabla b_\varepsilon + \text{Pe}\mathbf{v}_\varepsilon b_\varepsilon) = -\text{Da}_2 a_\varepsilon b_\varepsilon + \eta\text{Da}_3 c_\varepsilon, \tag{12b}$$
$$\partial_t c_\varepsilon + \nabla\cdot(-\mathbf{D}\nabla c_\varepsilon + \text{Pe}\mathbf{v}_\varepsilon c_\varepsilon) = \eta^{-1}\text{Da}_2 a_\varepsilon b_\varepsilon - \text{Da}_3 c_\varepsilon, \tag{12c}$$

where $\eta = \bar{c}/\hat{c}^\star$. The system (12) is subject to

$$\mathbf{n}\cdot\mathbf{D}\nabla a_\varepsilon = \mathbf{n}\cdot\mathbf{D}\nabla b_\varepsilon = 0, \quad -\mathbf{n}\cdot\mathbf{D}\nabla c_\varepsilon = \text{Da}_1(c_\varepsilon^n - 1), \quad \mathbf{x}\in\Gamma^\varepsilon, \quad t > 0. \tag{13}$$

The initial conditions read

$$a_\varepsilon(\mathbf{x},0) = a_{\text{in}}(\mathbf{x}), \quad b_\varepsilon(\mathbf{x},0) = b_{\text{in}}(\mathbf{x}), \quad c_\varepsilon(\mathbf{x},0) = c_{\text{in}}(\mathbf{x}). \tag{14}$$

3. Homogenization via multiple-scale expansions

We proceed by employing the method of multiple-scale expansions [2,19] to homogenize (upscale) the transport equations (10), (11), (12a)–(12c), (13) from the pore-scale to the macro-scale, and to derive effective equations for the average flow velocity $\langle\mathbf{v}_\varepsilon(\mathbf{x})\rangle$ and solutes' concentrations $\langle a_\varepsilon(\mathbf{x},t)\rangle, \langle b_\varepsilon(\mathbf{x},t)\rangle$, and $\langle c_\varepsilon(\mathbf{x},t)\rangle$.

In Section 3.1 we provide the relevant definitions and the general framework of the upscaling procedure. While the technical details of the derivation are presented in Appendix, the results of the homogenization procedure are summarized in Section 3.2. Here, we present a phase diagram identifying conditions under which the upscaled (macroscopic) system of equations is valid.

3.1. Preliminaries

Given any pore-scale quantity ψ_ε,

$$\langle\psi_\varepsilon\rangle \equiv \frac{1}{|Y|}\int_{\mathcal{B}(\mathbf{x})}\psi_\varepsilon d\mathbf{y}, \quad \langle\psi_\varepsilon\rangle_{\mathcal{B}} \equiv \frac{1}{|\mathcal{B}|}\int_{\mathcal{B}(\mathbf{x})}\psi_\varepsilon d\mathbf{y}, \text{ and}$$
$$\langle\psi_\varepsilon\rangle_\Gamma \equiv \frac{1}{|\Gamma|}\int_{\Gamma(\mathbf{x})}\psi_\varepsilon d\mathbf{y} \tag{15}$$

are three local averages (function of $\mathbf{x}$) over the pore space $\mathcal{B}(\mathbf{x})$ of the unit cell $Y(\mathbf{x})$ centred at $\mathbf{x}$. In (15), $\langle\psi_\varepsilon\rangle = \phi\langle\psi_\varepsilon\rangle_{\mathcal{B}}$ and $\phi = |\mathcal{B}|/|Y|$ is the porosity.

Within the framework of multiple-scale expansions method, we introduce a space variable $\mathbf{y}$ defined in the unit cell, i.e. $\mathbf{y}\in\mathcal{B}$, and four time variables. One of the four time variables is related to the advection time scale τ_{a}, while three are associated with the reactions time scales. The latter are represented by the vector $\boldsymbol{\tau}_{\text{r}}$ with components $[\boldsymbol{\tau}_{\text{r}}]_j = \tau_{\text{rj}}$, $j = \{1,2,3\}$. Each variable is defined as follows,

$$\mathbf{y} = \varepsilon^{-1}\mathbf{x}, \quad \tau_{\text{a}} = \text{Pe}\,t = \hat{t}_{\text{a}}^{-1}\hat{t}, \quad \text{and } \tau_{\text{rj}} = \text{Da}_j\,t = \hat{t}_{\text{rj}}^{-1}\hat{t}, \quad j = \{1,2,3\}. \tag{16}$$

Furthermore, any pore-scale function $\psi_\varepsilon(\mathbf{x},t)$ (e.g. concentration in (12)) is represented as $\psi_\varepsilon(\mathbf{x},t) := \psi(\mathbf{x},\mathbf{y},t,\tau_{\text{a}},\boldsymbol{\tau}_{\text{r}})$. Replacing $\psi_\varepsilon(\mathbf{x},t)$ with $\psi(\mathbf{x},\mathbf{y},t,\tau_{\text{a}},\boldsymbol{\tau}_{\text{r}})$ gives the following relations for the spatial and temporal derivatives,

$$\nabla\psi_\varepsilon = \nabla_{\mathbf{x}}\psi + \varepsilon^{-1}\nabla_{\mathbf{y}}\psi, \quad \text{and}$$
$$\frac{\partial\psi_\varepsilon}{\partial t} = \frac{\partial\psi}{\partial t} + \text{Pe}\frac{\partial\psi}{\partial\tau_{\text{a}}} + \text{Da}_j\frac{\partial\psi}{\partial\tau_{\text{rj}}}, \quad j = \{1,2,3\}, \tag{17}$$

respectively, where Einstein summation is implied whenever a repeated index is present. The function ψ is represented as an asymptotic series in powers of ε,

$$\psi(\mathbf{x},\mathbf{y},t,\tau_{\text{a}},\boldsymbol{\tau}_{\text{r}}) = \sum_{m=0}^{\infty}\varepsilon^m\psi_m(\mathbf{x},\mathbf{y},t,\tau_{\text{a}},\boldsymbol{\tau}_{\text{r}}), \tag{18}$$

wherein $\psi_m(\mathbf{x},\mathbf{y},t,\tau_{\text{a}},\boldsymbol{\tau}_{\text{r}}), m = 0,1,\ldots$, are Y-periodic in $\mathbf{y}$. Finally, we set

$$\text{Pe} = \varepsilon^{-\alpha}, \quad \text{Da}_1 = \varepsilon^{\beta}, \quad \text{Da}_2 = \varepsilon^{\gamma}, \quad \text{and Da}_3 = \varepsilon^{\delta} \tag{19}$$

with the exponents α, β, γ and δ determining the system behavior.

3.2. Upscaled transport equations and homogenizability conditions

The upscaling of Stokes equations 10 and 11 is a classical result of homogenization theory, e.g. [2,19,23, and references therein], and leads to Darcy's law and the continuity equation for the average velocity $\langle\mathbf{v}\rangle$, i.e.

$$\langle\mathbf{v}\rangle = -\mathbf{K}\cdot\nabla p_0, \quad \nabla\cdot\langle\mathbf{v}\rangle = 0, \quad \mathbf{x}\in\Omega, \tag{20}$$

where $\mathbf{K}$ is the dimensionless permeability tensor defined as the average, $\mathbf{K} = \langle\mathbf{k}(\mathbf{y})\rangle$, of the closure variable $\mathbf{k}(\mathbf{y})$, solution of a unit cell problem,

$$\nabla^2\mathbf{k} + \mathbf{I} - \nabla\mathbf{a} = \mathbf{0}, \quad \nabla\cdot\mathbf{k} = \mathbf{0}, \quad \mathbf{y}\in\mathcal{B}, \tag{21}$$

subject to the boundary condition $\mathbf{k}(\mathbf{y}) = \mathbf{0}$ for $\mathbf{y} \in \Gamma$, e.g. [2]. In (21), $\mathbf{a}$ is Y-periodic and satisfies the condition $\langle \mathbf{a} \rangle = \mathbf{0}$. See [19, pp. 46–47, Theorem 1.1] for a review.

In Appendix, we show that the pore-scale reactive transport processes described by (12) and (13) can be homogenized, i.e., approximated up to order ε^2, with an effective ADRE

$$\phi \partial_t \langle a \rangle_B = \nabla \cdot (\mathbf{D}^\star \nabla \langle a \rangle_B - \mathrm{Pe} \langle a \rangle_B \langle \mathbf{v} \rangle) - \phi \mathrm{Da}_2 \langle a \rangle_B \langle b \rangle_B + \phi \eta \mathrm{Da}_3 \langle c \rangle_B, \tag{22a}$$

$$\phi \partial_t \langle b \rangle_B = \nabla \cdot (\mathbf{D}^\star \nabla \langle b \rangle_B - \mathrm{Pe} \langle b \rangle_B \langle \mathbf{v} \rangle) - \phi \mathrm{Da}_2 \langle a \rangle_B \langle b \rangle_B + \phi \eta \mathrm{Da}_3 \langle c \rangle_B, \tag{22b}$$

$$\phi \partial_t \langle c \rangle_B = \nabla \cdot (\mathbf{D}^\star \nabla \langle c \rangle_B - \mathrm{Pe} \langle c \rangle_B \langle \mathbf{v} \rangle) + \phi \eta^{-1} \mathrm{Da}_2 \langle a \rangle_B \langle b \rangle_B - \phi \mathrm{Da}_3 \langle c \rangle_B - \varepsilon^{-1} \phi \mathrm{Da}_1 \mathcal{K}^\star (\langle c \rangle_B^n - 1), \tag{22c}$$

provided the following conditions are met:

(1) $\varepsilon \ll 1$,
(2) $\langle \boldsymbol{\chi} \rangle_\Gamma \approx \langle \boldsymbol{\chi} \rangle_B$,
(3) $\mathrm{Pe} < \varepsilon^{-2}$,
(4) $\mathrm{Da}_1 < 1$,
(5) $\mathrm{Da}_2 < \varepsilon^{-2}$,
(6) $\mathrm{Da}_3 < \varepsilon^{-2}$,
(7) $\mathrm{Da}_1/\mathrm{Pe} < \varepsilon$,
(8) $\mathrm{Da}_2/\mathrm{Pe} < \varepsilon^{-1}$,
(9) $\mathrm{Da}_3/\mathrm{Pe} < \varepsilon^{-1}$.

In (22), the dimensionless effective reaction rate constant, $\mathcal{K}^\star$, and dispersion tensor, $\mathbf{D}^\star$, are given by

$$\mathcal{K}^\star = \frac{|\Gamma|}{|\mathcal{B}|}, \quad \text{and } \mathbf{D}^\star = \langle \mathbf{D}(\mathbf{I} + \nabla_{\mathbf{y}} \boldsymbol{\chi}) \rangle + \varepsilon \mathrm{Pe} \langle \boldsymbol{\chi} \mathbf{k} \rangle \nabla_{\mathbf{x}} p_0, \tag{23}$$

where the closure variable $\boldsymbol{\chi}(\mathbf{y})$ has zero mean, $\langle \boldsymbol{\chi} \rangle = \mathbf{0}$, and is defined as a solution of the decoupled local problem

$$-\nabla_{\mathbf{y}} \cdot \mathbf{D}(\nabla_{\mathbf{y}} \boldsymbol{\chi} + \mathbf{I}) + \varepsilon \mathrm{Pe} \mathbf{v}_0 \nabla_{\mathbf{y}} \boldsymbol{\chi} = \varepsilon \mathrm{Pe} (\langle \mathbf{v}_0 \rangle_B - \mathbf{v}_0), \quad \mathbf{y} \in \mathcal{B}, \tag{24a}$$

$$-\mathbf{n} \cdot \mathbf{D}(\nabla_{\mathbf{y}} \boldsymbol{\chi} + \mathbf{I}) = 0, \quad \mathbf{y} \in \Gamma. \tag{24b}$$

Here, $\mathbf{v}_0 = -\mathbf{k} \cdot \nabla_{\mathbf{x}} p_0$ and the pressure p_0 is a solution of the effective flow equation (20).

Beside the classical constraint on geometrical scale-separation (constraint 1), and the operative constraint 2 which allows one to simplify the mathematical treatment for terms of the type $\langle \psi_1 \rangle_\Gamma$ (see Appendix A.3), the set of conditions 1–9 imposes bounds on the order of magnitude of the system's dimensionless numbers, and consequently on its dynamics, i.e. on the relative importance of advection, diffusion, linear and nonlinear homogeneous and heterogeneous reactions. Condition 3 requires that the system is not advection dominated at the pore-scale, and corresponds to the homogenizability contraint for a non-reacting tracer, as obtained by [2]. The upscaling of the nonlinear heterogeneous reaction requires additional constraints on the rate of reaction compared to both advection and diffusion processes, i.e. constraints 4 and 7. They correctly coincide with those identified by [5] for a simplified reactive system involving only species C. The constraint 4 imposes restrictions on the speed of the heterogeneous reactions compared to the diffusion process and guarantees that reaction-dominated conditions, characterized by narrow reacting fronts and high concentration gradients, do not occur at the pore-scale. It is worth noticing that the order n of the heterogeneous reaction does not play a role in defining the magnitude of the bounds 4 and 7. Therefore heterogeneous linear and nonlinear reactions share the same set of sufficient conditions for the applicability range of one-point closure upscaled equations, contrary to the common presumption that macroscopic equations are more robust if only linear reactions are involved in the system dynamics. Such sufficient conditions guarantee that the system is homogenized at the microscale and, consequently, there are no mass transport limitations at the pore-scale. A similar scenario holds for the nonlinear and linear homogeneous reactions, were the constraints 5 and 6 on Da_2 and Da_3, respectively, are identical although the nonlinear homogeneous reaction requires mixing between A and B to occur: an almost uniform concentration profile at the pore-scale is a sufficient condition for the reactants to be well-mixed, regardless of the type of reaction involved (linear or nonlinear, single- or multi-component). Similarly to condition 7, the additional constraints 8 and 9 impose conditions on the ratio between the advective and reactive timescales. Combining conditions 3 and 8 (or 9) leads to the constraints

$$\varepsilon \mathrm{Da}_2 < \mathrm{Pe} < \varepsilon^{-2} \quad \text{and} \quad \varepsilon \mathrm{Da}_3 < \mathrm{Pe} < \varepsilon^{-2},$$

which impose lower, as well as upper, bounds on the order of magnitude of Pe for any given $\mathrm{Da}_j < \varepsilon^{-2}$, $j = \{2, 3\}$. Importantly, the lower bounds require that advection is sufficiently faster than reaction processes (both homogeneous and heterogeneous), and reveal that advection can improve system homogenizability in presence of slow diffusion by enhancing pore-scale mixing and/or resupplying reactants removed by reactive processes. Also, the constraints related to the heterogeneous reaction, 4 and 7, are more stringent than those on the homogeneous reactions, 5, 6, 8 and 9. This can be attributed to the inherently local nature of heterogeneous reactions, which occur only in the vicinity of the solid–liquid interface.

It is worth noticing that while the choice of the macroscopic length scale L is, to some extent, arbitrary and non unique, this does not render the constraints 3–9 invalid. Given L such that $L > \ell$, or $\varepsilon := \ell/L < 1$, let us assume without loss of generality that the constraint 3 is satisfied, i.e. $\mathrm{Pe} := UL/\mathcal{D}_0 < \varepsilon^{-2}$. Let us pick a new macroscopic length scale, $\tilde{L} = qL$, where $q \geqslant 1$. Then, for this scenario, $\tilde{\varepsilon} := H/\tilde{L} = \varepsilon/q$, and $\tilde{\mathrm{Pe}} = q\mathrm{Pe}$. Since $\mathrm{Pe} < \varepsilon^{-2}$, then $\tilde{\mathrm{Pe}} < q\varepsilon^{-2}$ or, equivalently, $\tilde{\mathrm{Pe}} < \tilde{\varepsilon}^{-2}/q$. The latter condition implies $\tilde{\mathrm{Pe}} < \tilde{\varepsilon}^{-2}$ since $q \geqslant 1$, i.e. the sufficient condition 3 is still satisfied. Therefore, if $L > H$ and $\mathrm{Pe} < \varepsilon^{-2}$, then $\tilde{\mathrm{Pe}} < \tilde{\varepsilon}^{-2}$ for any $\tilde{L} \geqslant L$. A similar argument can be carried out for the remaining constraints.

These conditions can be graphically visualized in a phase diagram in the $(\mathrm{Pe}, \mathrm{Da}_j)$-space with $j = \{1, 2, 3\}$, or the $(\alpha, \beta, \gamma, \delta)$-space. For the sake of clarity and since the constraints on Da_2 and Da_3 (or γ and δ) coincide, we summarize the former conditions in the (α, β, γ)-space, only. In Fig. 1 the planes $\alpha = 2, \beta = 0$, and $\gamma = -2$ corresponds to $\mathrm{Pe} = \varepsilon^{-2}, \mathrm{Da}_1 = 1$, and $\mathrm{Da}_2 = \varepsilon^{-2}$, respectively; the half-spaces $\alpha + \beta > 1$ and $\alpha + \gamma > -1$ correspond to the constraints 7 and 8, respectively. These bounds identify a semi-infinite space, the coloured volume in Fig. 1, within which the sufficient conditions for homogenizability are satisfied. Fig. 1 generalizes the phase diagram developed by [5], which represents a cross-section of our phase diagram at $\mathrm{Da}_2 = 0$ and $\mathrm{Da}_3 = 0$ (or $\gamma \to +\infty$ and $\delta \to +\infty$, respectively). Outside such region the validity of local upscaled equations is not guaranteed to represent pore-scale processes within errors of order ε^2. Also, the patterns in Fig. 1 identify different transport regimes depending on the order of magnitude of Pe and Da_j as described in the following Section 4.

4. Special cases

In this section, we investigate how the system of upscaled Eq. (22), with effective coefficients defined by (23) and (24), can be further simplified in specific transport regimes. The latter are indicated by the differently patterned regions of Fig. 1. As previously discussed, the homogenizability constraints 1–9 require that the system is not reaction-dominated at the pore-scale. In the following we will therefore investigate diffusion- and advection-dominated regimes, and show that the system (22) correctly reduces to the conditions identified for non-reacting tracers [2], purely diffusive multi-component reactive systems [6], and single component advection–diffusion systems with nonlinear reaction [5].

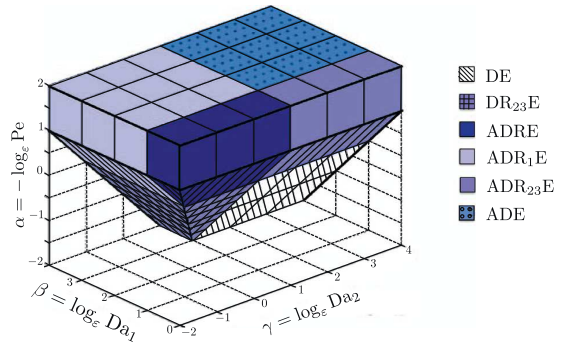

Fig. 1. Phase diagram indicating the range of applicability of macroscopic equations for the advection–reaction–diffusion system (12), (13) in terms of Pe and Da_j ($j = \{1,2,3\}$). The colored region identifies the sufficient conditions under which the macroscopic equations hold. In the white region, macro- and micro-scale problems are coupled and have to be solved simultaneously. Also, the patterns identify different transport regimes depending on the order of magnitude of Pe and Da_j as described in Section 4. Transport regimes where $\mathrm{Pe} < 1$ (Section 4.1), i.e. $\alpha < 0$, can be dominated by diffusion (region DE) or by diffusion and homogeneous reactions concurrently (region $\mathrm{DR}_{23}E$). In regimes where $1 \leqslant \mathrm{Pe} < \varepsilon^{-2}$ (Section 4.2), i.e. $0 \leqslant \alpha < 2$, advection cannot be neglected and transport processes are advective–dispersive if diffusion dominates reactions (ADE region), or advective–dispersive-reactive when homogeneous and/or heterogeneous reactions are not negligible (ADRE, ADR_1E and ADR_2E regions). Diffusion, advection, and reactions are of the same order of magnitude at the point $(\alpha,\beta,\gamma,\delta) = (1,0,-2,-2)$.

4.1. Transport regime with $\mathrm{Pe} < 1$

For small Péclet number, i.e. $\mathrm{Pe} < 1$, diffusion dominates advection at the continuum- and pore-scales. Therefore the system of equations (22) can be simplified to

$$\phi\partial_t\langle a\rangle_{\mathcal{B}} = \nabla\cdot(\mathbf{D}^\star\nabla\langle a\rangle_{\mathcal{B}}) - \phi\mathrm{Da}_2\langle a\rangle_{\mathcal{B}}\langle b\rangle_{\mathcal{B}} + \phi\eta\mathrm{Da}_3\langle c\rangle_{\mathcal{B}}, \tag{25a}$$

$$\phi\partial_t\langle b\rangle_{\mathcal{B}} = \nabla\cdot(\mathbf{D}^\star\nabla\langle b\rangle_{\mathcal{B}}) - \phi\mathrm{Da}_2\langle a\rangle_{\mathcal{B}}\langle b\rangle_{\mathcal{B}} + \phi\eta\mathrm{Da}_3\langle c\rangle_{\mathcal{B}}, \tag{25b}$$

$$\phi\partial_t\langle c\rangle_{\mathcal{B}} = \nabla\cdot(\mathbf{D}^\star\nabla\langle c\rangle_{\mathcal{B}}) + \phi\eta^{-1}\mathrm{Da}_2\langle a\rangle_{\mathcal{B}}\langle b\rangle_{\mathcal{B}} - \phi\mathrm{Da}_3\langle c\rangle_{\mathcal{B}} - \varepsilon^{-1}\phi\mathrm{Da}_1\mathcal{K}^\star(\langle c\rangle_{\mathcal{B}}^n - 1), \tag{25c}$$

with $\mathbf{D}^\star = \langle\mathbf{D}(\mathbf{I}+\nabla_{\mathbf{y}}\boldsymbol{\chi})\rangle$. The closure variable $\boldsymbol{\chi}$ is the solution of the following reduced closure problem:

$$-\nabla_{\mathbf{y}}\cdot\mathbf{D}(\nabla_{\mathbf{y}}\boldsymbol{\chi}+\mathbf{I}) = 0, \quad \mathbf{y}\in\mathcal{B}; \tag{26a}$$

$$-\mathbf{n}\cdot\mathbf{D}(\nabla_{\mathbf{y}}\boldsymbol{\chi}+\mathbf{I}) = 0, \quad \mathbf{y}\in\Gamma. \tag{26b}$$

Eqs. (25c) and (26) coincide with Eqs. (25) and (26) in [5, Section 4.1] for the diffusion-dominated transport regime of a single reactive species (i.e. $\mathrm{Da}_2 = \mathrm{Da}_3 = 0$) undergoing heterogeneous reaction. The order of magnitude of Da_j, $j = \{1,2,3\}$ determines the relative importance of the reactions compared to diffusion processes, as discussed in the following.

Diffusion dominates reactions, $\mathrm{Da}_j < \varepsilon, j = \{1,2,3\}$. In this regime diffusion dominates advection as well as all reactive transport processes at the macro-scale. Each species obeys a dispersion equation (DE) where all the reaction terms in (25) are negligible. Such transport regime is represented by the diagonally patterned (DE) region in Fig. 1. For a single component (i.e. $\mathrm{Da}_2 = \mathrm{Da}_3 = 0$) undergoing nonlinear heterogeneous reactions, results from [5, Eq. 27] are recovered.

Diffusion and homogeneous reactions are comparable, $\mathrm{Da}_1 < \varepsilon$, $\varepsilon \leqslant \mathrm{Da}_j < \varepsilon^{-1}, j = \{2,3\}$. In this regime ($\mathrm{DR}_{23}$E region in Fig. 1), the heterogeneous reaction is negligible compared to other transport mechanisms. As a result, the corresponding reaction term in Eq. (25c) can be neglected. On the other hand, the homogeneous reactions cannot be neglected since $\varepsilon < \mathrm{Da}_{2,3} \leqslant \varepsilon^{-1}$.

4.2. Transport regimes with $1 \leqslant \mathrm{Pe} < \varepsilon^{-2}$

For $1 \leqslant \mathrm{Pe} < \varepsilon^{-2}$, advection cannot be neglected at the macroscale and advection terms have to be retained in Eq. (22). For $\varepsilon^{-1} \leqslant \mathrm{Pe} < \varepsilon^{-2}$, advection and diffusion are of the same order of magnitude at the pore-scale as well, and (24) must be employed. If, on the other hand, $1 \leqslant \mathrm{Pe} < \varepsilon^{-1}$ (vertically striped region in Fig. 1), advection becomes negligible at the microscale, and the closure problem can be simplified to (26). As a result, the effective coefficient $\mathbf{D}^\star$ to be employed in (22) must be obtained from the solution of the appropriate closure problem (24) or (26), if $\varepsilon^{-1} \leqslant \mathrm{Pe} < \varepsilon^{-2}$ or $1 \leqslant \mathrm{Pe} < \varepsilon^{-1}$, respectively. The impact of Da_j is discussed in the following.

Diffusion and reactions are comparable, $\varepsilon \leqslant \mathrm{Da}_1 < 1$, $2\varepsilon \leqslant \mathrm{Da}_j < \varepsilon^{-2}, j = \{2,3\}$. In this regime (region ADRE in Fig. 1), all the transport mechanisms are of the same order, and (22) must be employed.

Diffusion and heterogeneous reaction are comparable, and dominate homogeneous reactions, $\varepsilon \leqslant \mathrm{Da}_1 < 1, \mathrm{Da}_j < \varepsilon, j = \{2,3\}$. In this regime (region ADR_1E in Fig. 1), the homogeneous reaction terms can be neglected in (22), while the heterogeneous reaction term in (22c) has to be retained. No coupling between species holds, since $\langle a\rangle$ and $\langle b\rangle$ behave as nonreactive tracers undergoing advection and dispersion, whereas $\langle c\rangle$ obeys its own advection–dispersion-reaction equation as in [5, Section 4.2], and is produced (or consumed) only through dissolution (or precipitation) processes at the solid–liquid boundary.

Diffusion and homogeneous reactions are comparable, and dominate heterogeneous reactions, $\mathrm{Da}_1 < \varepsilon, \varepsilon \leqslant \mathrm{Da}_j < \varepsilon^{-2}, j = \{2,3\}$. In this regime (region ADR_{23}E in Fig. 1), heterogeneous reactions are characterized by a slow kinetics and can be neglected in (22c), while homogeneous reaction terms are not negligible.

Diffusion dominates reactions, $\mathrm{Da}_j < \varepsilon, j = \{1,2,3\}$. In this regime (region ADE in Fig. 1), transport can be modeled separately for each species, since both homogeneous and heterogeneous reactions are negligible. The transport of each species at the continuum-scale can be modeled by advection–dispersion equations decoupled from each other. The resulting equations correspond to the macroscopic equation for a tracer undergoing diffusion and advection, as described in [2]. In this scenario, constraints 7–9 are automatically fulfilled.

5. Reactive flow through a planar fracture

In this section we employ numerical simulations, both at the pore- and macro-scale, to test the sufficient conditions 1–9. We consider a pressure-driven flow through a bidimensional fracture $\Omega = \{(x,y): x\in(0,1), |y| < \varepsilon\}$ of width 2ε and unitary length, with solid boundary $\Gamma^\varepsilon = \{(x,y): x\in(0,1), y = \pm\varepsilon\}$. We assume that the precipitation/dissolution process does not significantly affect the interface Γ^ε, and the evolution of the solid–liquid boundary needs not to be taken into account. For a fracture of width H, the length L is to be interpreted as the "observation scale" [23]. In all the numerical simulations we set $\varepsilon := H/L = 6.25\cdot10^{-3}$.

5.1. Flow and transport equations

Fully developed flow within a planar fracture Ω is characterized by a pore-scale velocity $\mathbf{v}(y) = [v(y)\,0]$, with

$$\mathbf{v}(y) = \frac{3}{2}\left[1 - \left(\frac{y}{\varepsilon}\right)^2\right], \quad \text{for } y \leqslant |\varepsilon|. \tag{27}$$

The pore-scale transport Eq. (12) reduce to

$$\partial_t a_\varepsilon - D(\partial_{xx}a_\varepsilon + \partial_{yy}a_\varepsilon) + \mathrm{Pe}\, v(y)\partial_x a_\varepsilon = -\mathrm{Da}_2 a_\varepsilon b_\varepsilon + \eta \mathrm{Da}_3 c_\varepsilon, \quad (28a)$$

$$\partial_t b_\varepsilon - D(\partial_{xx}b_\varepsilon + \partial_{yy}b_\varepsilon) + \mathrm{Pe}\, v(y)\partial_x b_\varepsilon = -\mathrm{Da}_2 a_\varepsilon b_\varepsilon + \eta \mathrm{Da}_3 c_\varepsilon, \quad (28b)$$

$$\partial_t c_\varepsilon - D(\partial_{xx}c_\varepsilon + \partial_{yy}c_\varepsilon) + \mathrm{Pe}\, v(y)\partial_x c_\varepsilon = \eta^{-1}\mathrm{Da}_2 a_\varepsilon b_\varepsilon - \mathrm{Da}_3 c_\varepsilon, \quad (28c)$$

subject to

$$\partial_y a_\varepsilon = \partial_y b_\varepsilon = 0, \quad -D\partial_y c_\varepsilon = \mathrm{Da}_1(c_\varepsilon^n - 1), \quad \mathbf{x} \in \Gamma^\varepsilon,\ t > 0. \quad (29)$$

In Eqs. (28) and (29), we set $n = 1$ and $\eta = 1$. Species A and B are spatially separated at $t = 0$. We set the position of the initial concentration discontinuity at $\bar{x} = 0.25$. Since species A and B are not mixed at $t = 0$, the initial concentration of the product C is zero, and the initial conditions for $a_\varepsilon, b_\varepsilon$ and c_ε are:

$$a_\varepsilon(x \leqslant \bar{x}, y, t = 0) = 1, \quad a_\varepsilon(x > \bar{x}, y, t = 0) = 0, \quad (30a)$$

$$b_\varepsilon(x \leqslant \bar{x}, y, t = 0) = 0, \quad b_\varepsilon(x > \bar{x}, y, t = 0) = 1, \quad (30b)$$

$$c_\varepsilon(x, y, t = 0) = 0. \quad (30c)$$

Additionally, the following boundary conditions are imposed at the fracture inlet ($x = 0$) and outlet ($x = 1$):

$$a_\varepsilon(0, y, t) = 1, \quad \partial_x a_\varepsilon(1, y, t) = 0 \quad (31a)$$

$$b_\varepsilon(1, y, t) = 1, \quad \partial_x b_\varepsilon(0, y, t) = 0 \quad (31b)$$

$$\partial_x c_\varepsilon(0, y, t) = 0, \quad \partial_x c_\varepsilon(1, y, t) = 0. \quad (31c)$$

From any pore-scale quantity ψ_ε, the corresponding macroscopic quantity $\langle\psi\rangle$ is determined as follows,

$$\langle\psi\rangle_B(x, t) = \frac{1}{2\varepsilon}\int_{-\varepsilon}^{\varepsilon} \psi_\varepsilon(x, y, t)dy. \quad (32)$$

The transport equations (22) for the upscaled concentrations $\langle a\rangle_B, \langle b\rangle_B$ and $\langle c\rangle_B$ simplify to

$$\partial_t\langle a\rangle_B - D^\star\partial_{xx}\langle a\rangle_B + \mathrm{Pe}\partial_x\langle a\rangle_B = -\mathrm{Da}_2\langle a\rangle_B\langle b\rangle_B + \mathrm{Da}_3\langle c\rangle_B, \quad (33a)$$

$$\partial_t\langle b\rangle_B - D^\star\partial_{xx}\langle b\rangle_B + \mathrm{Pe}\partial_x\langle b\rangle_B = -\mathrm{Da}_2\langle a\rangle_B\langle b\rangle_B + \mathrm{Da}_3\langle c\rangle_B, \quad (33b)$$

$$\partial_t\langle c\rangle_B - D^\star\partial_{xx}\langle c\rangle_B + \mathrm{Pe}\partial_x\langle c\rangle_B = \mathrm{Da}_2\langle a\rangle_B\langle b\rangle_B - \mathrm{Da}_3\langle c\rangle_B - \varepsilon^{-1}\mathrm{Da}_1\mathcal{K}^\star(\langle c\rangle_B - 1), \quad (33c)$$

since $\phi = 1, \eta = 1, n = 1$, and $\langle v(y)\rangle = 1$. In (33),

$$\mathcal{K}^\star = 1 \quad \text{and } D^\star = D + \frac{2}{105}\frac{(\varepsilon\mathrm{Pe})^2}{D}. \quad (34)$$

The effective dispersion coefficient, $D^\star$, is analytically determined by solving a simplified pore-scale problem (24) [23, Eq. (69)]. The impact of sub-scale velocity non-uniformities on $D^\star$ is reflected by the impact of Pe number: the bigger Pe the bigger the deviations of $D^\star$ from D. Eqs. (33) are subject to initial conditions

$$\langle a\rangle_B(x \leqslant \bar{x}, y, t = 0) = \langle b\rangle_B(x > \bar{x}, y, t = 0) = 1, \quad (35a)$$

$$\langle a\rangle_B(x > \bar{x}, y, t = 0) = \langle b\rangle_B(x \leqslant \bar{x}, y, t = 0) = \langle c\rangle_B(x, y, t = 0) = 0, \quad (35b)$$

and boundary conditions

$$\partial_x\langle a\rangle_B(0, y, t) = \partial_x\langle b\rangle_B(1, y, t) = \partial_x\langle c\rangle_B(0, y, t) = \partial_x\langle c\rangle_B(1, y, t) = 0, \quad (36a)$$

$$\langle a\rangle_B(0, y, t) = \langle b\rangle_B(1, y, t) = 1, \quad \langle c\rangle_B(0, y, t) = \langle c\rangle_B(1, y, t) = 0. \quad (36b)$$

The numerical solution of (28) and (33) subject to (29)–(31) and (35), (36), respectively, is achieved by means of smoothed particle hydrodynamics (SPH) simulations, a fully Lagrangian particle method.While originally developed in the context of astrophysical applications, SPH has been successfully used to model (unsaturated, saturated and multiphase) flows and (non-) reactive transport in the subsurface at the micro-scale, e.g. [29,30], as well as at the continuum-scale [10,17]. Both the pore- and continuum-scale system of equations (28) and (33) are solved with a longitudinal spatial resolution $\Delta x = 2.5 \cdot 10^{-4}$.An explicit time-marching scheme imposes that the time steps, $\Delta t = 0.1h^2/\tilde{D}$, with $\tilde{D} = D$ or $\tilde{D} = D^\star$ for pore- and continuum-scale systems, respectively, and h a smoothing length assigned as a function of the mean particle distance, satisfy the Courant-Friedrichs-Lewy (CFL) condition, see [29] for details. A set of parameters used in the numerical solutions of (28) and (33) is listed in Table1. For details regarding the numerical implementation of the complete reactive problem, see [29, and references therein].

5.2. Simulation results

In this section we present the results of numerical simulations for different combinations of $(\alpha, \beta, \gamma, \delta)$ to investigate the robustness of the homogenizability conditions 3–9. We consider five different test cases, whose parameter values are listed in Table 2. Case 1 and 2 satisfy the constraints 3–9, while cases 3, 4 and 5 violate one or more conditions for homogenizability. For each scenario, we compare macroscale concentration profiles along the fracture $\langle\psi\rangle_{B,\mathrm{M}}, \psi = \{a, b, c\}$, obtained by solving the continuum-scale system (33), with the spatially averaged microscale concentration fields $\langle\psi\rangle_{B,\mathrm{m}}$ calculated by numerical integration of pore-scale concentration profiles ψ_ε according to (32). Inside the homogenizability region, the solution of (33) is expected to be within errors $\mathcal{O}(\varepsilon^2)$ from the averaged pore-scale solution, i.e. $\langle\psi\rangle_{B,\mathrm{m}} = \langle\psi\rangle_{B,\mathrm{M}} + \mathcal{O}(\varepsilon^2)$, or the absolute error $E_\psi = |\langle\psi\rangle_{B,\mathrm{m}} - \langle\psi\rangle_{B,\mathrm{M}}| \approx \mathcal{O}(\varepsilon^2)$.

The parameter values of the first scenario (Case 1 in Table 2) satisfy the homogenizability conditions. Fig. 2(i) shows the longitudinal profiles for the averaged concentration of each species. Grey lines represent the averaged microscale solution $\langle\psi\rangle_{B,\mathrm{m}}, \psi = \{a, b, c\}$, whereas black lines refer to the macroscale solution $\langle\psi\rangle_{B,\mathrm{M}}$. As predicted by homogenization theory, the absolute errors along the fracture $E_\psi, \psi = \{a, b, c\}$, are of order ε^2 (Fig. 2(ii)). Errors are larger across the initial concentration discontinuity where the concentration gradients are the highest. The production of species C is concentrated around the mixing front between A and B, as shown in Figs. 2(iii), whereas C production along the fracture boundaries is negligible because of relatively slow heterogeneous reaction kinetics, i.e. relatively big β. This results in a well-mixed system due to strong transversal mixing, i.e. $\psi_\varepsilon(x, y) \approx \psi_\varepsilon(x), \psi = \{a, b, c\}$.

Table 1
SPH simulation parameters.

	Pore-scale	Continuum-scale
Δx	$2.5 \cdot 10^{-4}$	$2.5 \cdot 10^{-4}$
Δy	$2.5 \cdot 10^{-4}$	n/a
h	$5 \cdot 10^{-4}$	$5 \cdot 10^{-4}$

Table 2
Simulation scenarios considered in this study with corresponding values of α, β, γ, and δ. Case 1 and 2 satisfy all the homogenizability conditions 3–9. Case 3, 4 and 5 violate at least one of the sufficient conditions for homogenizability. The parameters' values that do not satisfy the constraints are highlighted in boldface.

	Case 1	Case 2	Case 3	Case 4	Case 5
α	1	1	1/2	1	1/2
β	1	1/4	1/4	**−1**	1
γ	−7/4	−1	−1	−1	−7/4
δ	−7/4	−1	−1	−1	−7/4
$\alpha+\beta$	2	5/4	**3/4**	**0**	3/2
$\alpha+\gamma$	−3/4	0	−1/2	0	**−5/4**
$\alpha+\delta$	−3/4	0	−1/2	0	**−5/4**

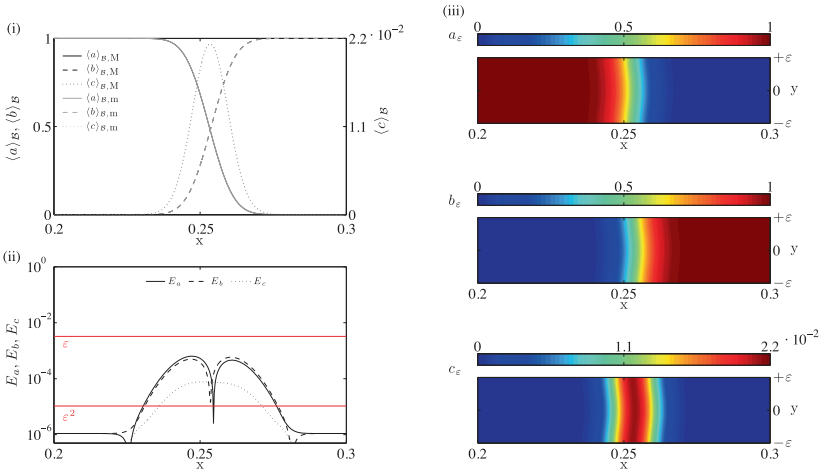

Fig. 2. Test Case 1 with $(\alpha,\beta,\gamma,\delta) = (1,1,-7/4,-7/4)$. Snapshot of $\langle\psi\rangle_{\mathcal{B},\mathrm{M}}$ (black lines) and $\langle\psi\rangle_{\mathcal{B},\mathrm{m}}$ (gray lines) with $\psi = \{a,b,c\}$ at time $t = \varepsilon^{\alpha}$. (i) Longitudinal concentration profiles $\langle\psi\rangle_{\mathcal{B},\mathrm{M}}$ and $\langle\psi\rangle_{\mathcal{B},\mathrm{m}}$ obtained from either solving the macroscale system of equations (33), or averaging the pore-scale concentration profiles, respectively. (ii) Absolute error along the fracture $E_\psi(x) = |\langle\psi\rangle_{\mathcal{B},\mathrm{m}}(x) - \langle\psi\rangle_{\mathcal{B},\mathrm{M}}(x)|$. Red horizontal lines identify different orders of magnitude of the absolute error in terms of integer powers of ε. (iii) Concentration maps in a portion of the fracture, $x \in [0.2, 0.3]$ and $y = [-\varepsilon, \varepsilon]$, for species A (top), B (middle) and C (bottom) around the original concentration discontinuity $\bar{x} = 0.25$.

Case 2, with $(\alpha,\beta,\gamma,\delta) = (1,1/4,-1,-1)$, satisfies the homogenizability conditions and corresponds to a scenario where the heterogeneous reaction is faster, i.e. β is smaller, while the homogeneous reactions are slower, i.e. γ and δ are larger, than in Case 1. Fig. 3(i) and (ii) show the longitudinal concentration and absolute error profiles for the three species, respectively. The absolute error $E_\psi, \psi = \{a,b,c\}$ is bounded by ε, as expected. A faster heterogeneous reaction leads to an accumulation of C close to the solid boundaries as showed in Fig. 3(iii). Further, since the homogeneous reactions are slower compared to Case 1, there is only negligible accumulation of C at locations in proximity of $x = 0.25$. This is because A and B diffuse away from the original concentration discontinuity at $x = 0.25$ more quickly than in Case 1, and before the homogeneous reaction to form C goes to completion. This translates in a lower maximum c_ε compared to Case 1, and in the appearance of mild nonlocal effects, i.e. C production in areas other than those where mixing between A and B originally occurs.

Case 3 shares the same set of parameters with Case 2, except for a lower value of α, corresponding to slower advection at the micro-scale. Contrary to intuition, a slower advection drags the system outside the homogenizability regime, since constraint 7 is now violated. Slower advection results in an increased longitudinal, rather than transversal, mixing, as showed in Fig. 4(iii), where the width of the diffusion and reaction fronts is much wider than in Fig. 4(iii). The appearance of significant nonlocal effects, i.e. stronger longitudinal mixing to the detriment of transversal one, is accentuated by C production at the solid boundaries. As a result, the errors $E_\psi > \varepsilon$ (see Fig. 4(ii)), and the macroscopic equation significantly underestimates C production, Fig. 4 (i). This suggests that advection can act as a physical mechanism which enhances transversal mixing in presence of relatively slow diffusion.

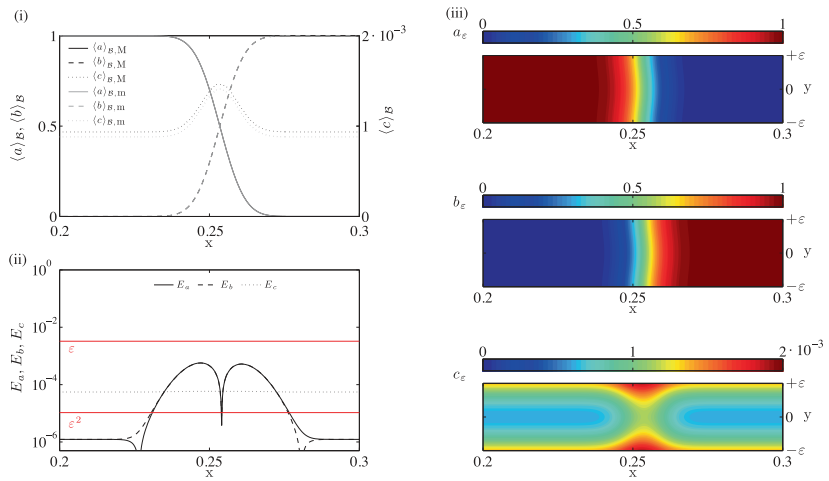

Fig. 3. Test Case 2 with $(\alpha,\beta,\gamma,\delta) = (1,1/4,-1,-1)$. Snapshot of $\langle\psi\rangle_{\mathcal{B},\mathrm{M}}$ (black lines) and $\langle\psi\rangle_{\mathcal{B},\mathrm{m}}$ (gray lines) with $\psi = \{a,b,c\}$ at time $t = \varepsilon^{\alpha}$. (i) Longitudinal concentration profiles $\langle\psi\rangle_{\mathcal{B},\mathrm{M}}$ and $\langle\psi\rangle_{\mathcal{B},\mathrm{m}}$ obtained from either solving the macroscale system of equations (33), or averaging the pore-scale concentration profiles, respectively. (ii) Absolute error along the fracture $E_\psi(x) = |\langle\psi\rangle_{\mathcal{B},\mathrm{m}}(x) - \langle\psi\rangle_{\mathcal{B},\mathrm{M}}(x)|$. Red horizontal lines identify different orders of magnitude of the absolute error in terms of integer powers of ε. (iii) Concentration maps in a portion of the fracture, $x \in [0.2, 0.3]$ and $y = [-\varepsilon, \varepsilon]$, for species A (top), B (middle) and C (bottom) around the original concentration discontinuity $\bar{x} = 0.25$.

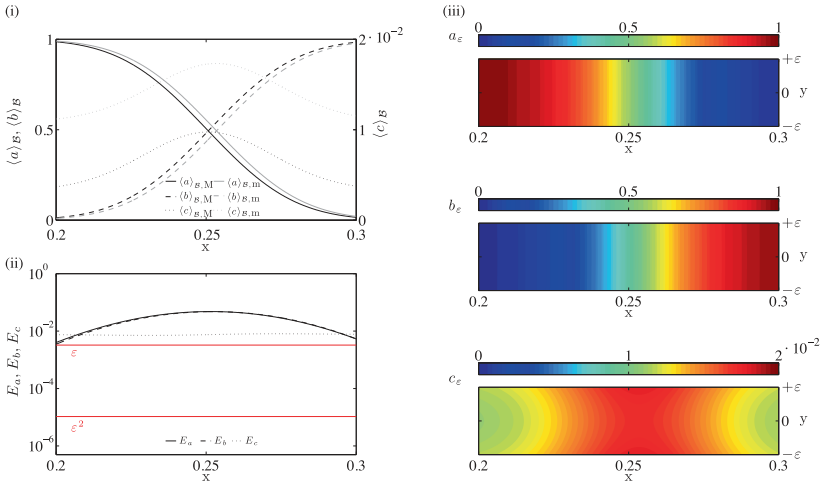

Fig. 4. Test Case 3 with $(\alpha,\beta,\gamma,\delta)=(1/2,1/4,-1,-1)$. Snapshot of $\langle\psi\rangle_{\mathcal{B},\mathrm{M}}$ (black lines) and $\langle\psi\rangle_{\mathcal{B},\mathrm{m}}$ (gray lines) with $\psi=\{a,b,c\}$ at time $t=\varepsilon^{\alpha}$. (i) Longitudinal concentration profiles $\langle\psi\rangle_{\mathcal{B},\mathrm{M}}$ and $\langle\psi\rangle_{\mathcal{B},\mathrm{m}}$ obtained from either solving the macroscale system of equations (33), or averaging the pore-scale concentration profiles, respectively. (ii) Absolute error along the fracture $E_\psi(x)=|\langle\psi\rangle_{\mathcal{B},\mathrm{m}}(x)-\langle\psi\rangle_{\mathcal{B},\mathrm{M}}(x)|$. Red horizontal lines identify different orders of magnitude of the absolute error in terms of integer powers of ε. (iii) Concentration maps in a portion of the fracture, $x\in[0.2,0.3]$ and $y=[-\varepsilon,\varepsilon]$, for species A (top), B (middle) and C (bottom) around the original concentration discontinuity $\bar{x}=0.25$.

An increase in the heterogeneous reaction rate compared to Case 2 leads to a reaction-driven regime at the microscale, i.e. $\beta<0$, which drives the system outside the homogenizability region (Case 4). At the pore-scale, the production of C from dissolution of the fracture boundary dominates its production due to mixing of A and B (Fig. 5(iii)). Therefore, C is not concentrated around the discontinuity front, and is poorly mixed in the transversal direction, i.e. $c_\varepsilon(x,y)\approx c_\varepsilon(y)$. As a result, the continuum-scale solution $\langle c\rangle_{\mathcal{B},\mathrm{M}}$ significantly overestimates the actual value of the averaged pore-scale concentration $\langle c\rangle_{\mathcal{B},\mathrm{m}}$ (Fig. 5(i)). This leads to $E_c>\varepsilon$ along the fracture, while E_a and E_b are still bounded by ε, as showed in Fig. 5(ii). It is worth noticing that failed mixing at the pore-scale (i.e. in the y-direction) leads to a global breakdown of the continuum-scale solution, i.e. $E_c(x)>\varepsilon$ for any x.

The last test case (Case 5) exhibits the same set of parameters as Case 1, except for a slower advection, i.e. smaller α. Similarly to Case 3, a slower advection drives the system outside the homogenizability regime, and translates into wider diffusive and reacting fronts, as showed in Fig. 6(iii). The product C diffuses longitudinally along the fracture much more efficiently: this leads to an averaged microscopic concentration $\langle c\rangle_{\mathcal{B},\mathrm{m}}$ with a nearly uniform profile (see Fig. 6.(i)) along the fracture, compared to its macroscopic value $\langle c\rangle_{\mathcal{B},\mathrm{M}}$ which cannot properly capture C longitudinal diffusion after its production due to mixing of A and B. Fig. 6(i) shows that the macroscopic equation significantly overestimates $\langle c_\varepsilon\rangle$, while

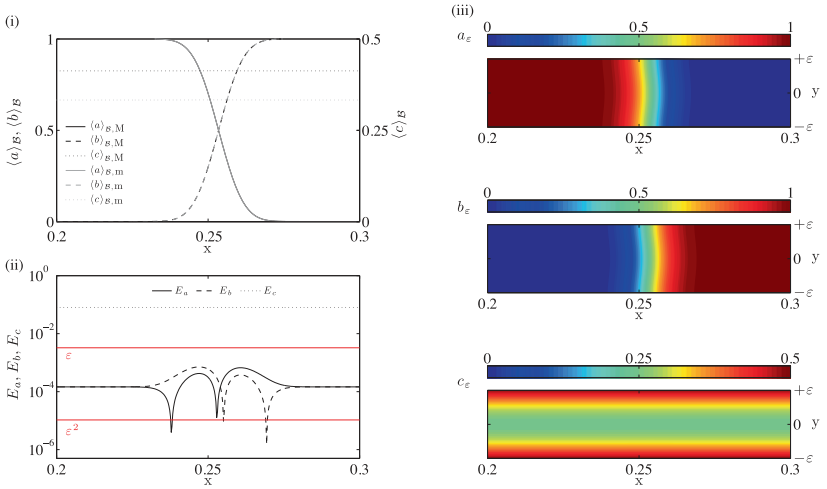

Fig. 5. Test Case 4 with $(\alpha,\beta,\gamma,\delta)=(1,-1,-1,-1)$. Snapshot of $\langle\psi\rangle_{\mathcal{B},\mathrm{M}}$ (black lines) and $\langle\psi\rangle_{\mathcal{B},\mathrm{m}}$ (gray lines) with $\psi=\{a,b,c\}$ at time $t=\varepsilon^{\alpha}$. (i) Longitudinal concentration profiles $\langle\psi\rangle_{\mathcal{B},\mathrm{M}}$ and $\langle\psi\rangle_{\mathcal{B},\mathrm{m}}$ obtained from either solving the macroscale system of equations (33), or averaging the pore-scale concentration profiles, respectively. (ii) Absolute error along the fracture $E_\psi(x)=|\langle\psi\rangle_{\mathcal{B},\mathrm{m}}(x)-\langle\psi\rangle_{\mathcal{B},\mathrm{M}}(x)|$. Red horizontal lines identify different orders of magnitude of the absolute error in terms of integer powers of ε. (iii) Concentration maps in a portion of the fracture, $x\in[0.2,0.3]$ and $y=[-\varepsilon,\varepsilon]$, for species A (top), B (middle) and C (bottom) around the original concentration discontinuity $\bar{x}=0.25$.

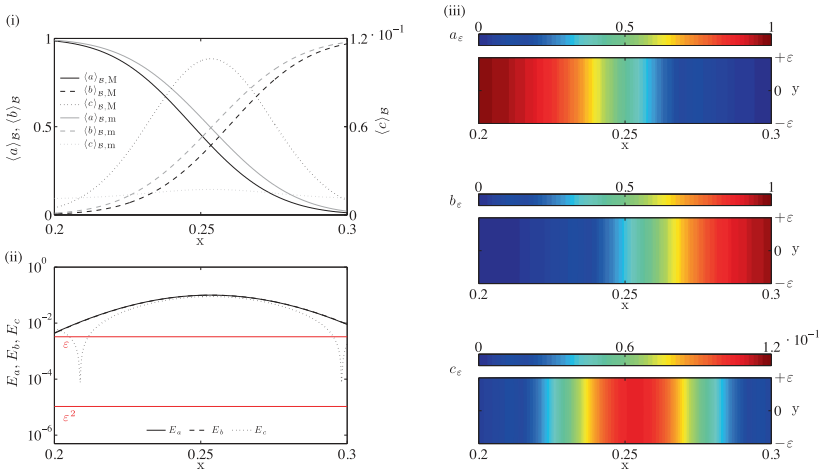

Fig. 6. Test Case 5 with $(\alpha,\beta,\gamma,\delta)=(1/2,1,-7/4,-7/4)$. Snapshot of $\langle\psi\rangle_{\mathcal{B},\mathrm{M}}$ (black lines) and $\langle\psi\rangle_{\mathcal{B},\mathrm{m}}$ (gray lines) with $\psi=\{a,b,c\}$ at time $t=\varepsilon^2$. (i) Longitudinal concentration profiles $\langle\psi\rangle_{\mathcal{B},\mathrm{M}}$ and $\langle\psi\rangle_{\mathcal{B},\mathrm{m}}$ obtained from either solving the macroscale system of equations (33), or averaging the pore-scale concentration profiles, respectively. (ii) Absolute error along the fracture $E_\psi(x)=|\langle\psi\rangle_{\mathcal{B},\mathrm{m}}(x)-\langle\psi\rangle_{\mathcal{B},\mathrm{M}}(x)|$. Red horizontal lines identify different orders of magnitude of the absolute error in terms of integer powers of ε. (iii) Concentration maps in a portion of the fracture, $x\in[0.2,0.3]$ and $y=[-\varepsilon,\varepsilon]$, for species A (top), B (middle) and C (bottom) around the original concentration discontinuity $\bar{x}=0.25$.

underestimating both $\langle a_\varepsilon\rangle$ and $\langle b_\varepsilon\rangle$. The errors, plotted in Fig. 6(ii), are greater than ε.

It is worth noticing that, despite constraints 1–9 represent sufficient conditions, they appear extremely robust in identifying necessary conditions for homogenizability.

6. Conclusions

Reactive transport in the subsurface involves coupled multicomponent systems where both nonlinear/linear homogeneous and heterogeneous reactions occur. Such systems have challenged classical local (one-point closure) macroscopic (continuum-scale) models, which fail to capture a number of critical transport features, including accurate location of reacting fronts, and amount of reacting products, just to mention a few. While such shortcomings have drawn the interest of the scientific community towards more robust modeling techniques (e.g. non-local multi-point closure approaches, hybrid and multiscale models), the conditions under which the latter are necessary are still subject of current investigations.

In this work we considered multicomponent reactive transport in porous media with three species undergoing a fully reversible mixing-controlled precipitation/dissolution process involving a homogeneous reaction, $A+B\rightleftharpoons C$, and a heterogeneous reaction, $C\rightleftharpoons S$ on the solid–liquid interface. By means of multiple-scale expansions, we established sufficient conditions under which macroscopic local advection–dispersion-reaction equations (ADREs) provide an accurate representation of pore-scale processes. Such conditions can be expressed as bounds on Péclet (Pe) and three Damköhler (Da_j, $j=\{1,2,3\}$) numbers, which quantify the relative importance of the four key mechanisms involved in the transport process, i.e. advection, molecular diffusion, homogeneous and heterogeneous reactions. Such a set of conditions delimits a homogenizability region in a (Pe,Da_j)-phase diagram (Fig. 1), where the pore-scale reactive transport processes can be homogenized, i.e. approximated up to order ε^2, with an effective ADRE, and the effective coefficients in the upscaled equations can be determined by solving a closure problem fully decoupled from the transport dynamics at the microscale. Whenever the coupling between micro- and macro-scale occurs, it is not guaranteed that the ADREs will accurately describe pore-scale processes within errors of order ε^2. Additionally, we verified the previously derived conditions through pore-scale numerical simulations of multicomponent transport in a planar fracture with reacting walls. Our major conclusions can be summarized as follows:

(1) Our conditions are consistent with the results of [5], in the absence of advection, and with the limits individuated by [2], in the absence of reactions;
(2) Heterogeneous reaction imposes more severe constraints on the system dynamics than homogeneous ones, since the former are localized on the solid–liquid boundaries;
(3) In a planar fracture, stronger advection can act as a physical mechanism which enhances transversal mixing in presence of relatively slow diffusion.
(4) Numerical simulations for reactive flow through a planar fracture suggest that the constraints derived in our analysis appear robust in identifying sufficient as well as necessary conditions for homogenizability.

Appendix A. Homogenization of transport equations

For convenience and compactness, we upscale only the governing equation for a_ε. The other two equations are upscaled in a similar fashion. Derivations related to c_ε will be made explicit only whenever its upscaling significantly differs from that of a_ε.

Let us represent $\psi_\varepsilon(\mathbf{x},t)$ as $\psi_\varepsilon(\mathbf{x},t):=\psi(\mathbf{x},\mathbf{y},t,\tau_\mathrm{a},\tau_\mathrm{r})$, $\psi=\{a,b,c\}$. Inserting (17) in (12a) and the first of (13), we obtain

$$\partial_t a+\mathrm{Pe}\partial_{\tau_a}a+\mathrm{Da}_j\partial_{\tau_{rj}}a+\nabla_{\mathbf{x}}\cdot[-\mathbf{D}(\nabla_{\mathbf{x}}a+\varepsilon^{-1}\nabla_{\mathbf{y}}a)+\mathrm{Pe}\mathbf{v}a]$$
$$+\varepsilon^{-1}\nabla_{\mathbf{y}}\cdot[-\mathbf{D}(\nabla_{\mathbf{x}}a+\varepsilon^{-1}\nabla_{\mathbf{y}}a)+\mathrm{Pe}\mathbf{v}a]+\mathrm{Da}_2ab-\eta\mathrm{Da}_3c=0,\quad \mathbf{y}\in\mathcal{B},\tag{A.1}$$

subject to

$$\mathbf{n}\cdot[\mathbf{D}(\nabla_{\mathbf{x}}a+\varepsilon^{-1}\nabla_{\mathbf{y}}a)]=0,\quad \mathbf{y}\in\Gamma.\tag{A.2}$$

For species C, combining (12c) with (17) leads to

$$\partial_t c+\mathrm{Pe}\partial_{\tau_a}c+\mathrm{Da}_j\partial_{\tau_{rj}}c+\nabla_{\mathbf{x}}\cdot[-\mathbf{D}(\nabla_{\mathbf{x}}c+\varepsilon^{-1}\nabla_{\mathbf{y}}c)+\mathrm{Pe}\mathbf{v}c]$$
$$+\varepsilon^{-1}\nabla_{\mathbf{y}}\cdot[-\mathbf{D}(\nabla_{\mathbf{x}}c+\varepsilon^{-1}\nabla_{\mathbf{y}}c)+\mathrm{Pe}\mathbf{v}c]-\eta^{-1}\mathrm{Da}_2ab+\mathrm{Da}_3c=0,\quad \mathbf{y}\in\mathcal{B},\tag{A.3}$$

subject to the boundary condition

$$\mathbf{n}\cdot[\mathbf{D}(\nabla_{\mathbf{x}}c+\varepsilon^{-1}\nabla_{\mathbf{y}}c)]=\mathrm{Da}_1(c^n-1),\quad \mathbf{y}\in\Gamma. \tag{A.4}$$

We insert the ansatz (18) in A.1,A.2, and collect like-power of ε. We obtain

$$\begin{aligned}&\varepsilon^{-2}\{\nabla_{\mathbf{y}}\cdot(-\mathbf{D}\nabla_{\mathbf{y}}a_0+\varepsilon^{1-\alpha}a_0\mathbf{v}_0)+\varepsilon^{2+\gamma}(\partial_{\tau_{r2}}a_0+a_0b_0)\\&\quad+\varepsilon^{2+\delta}(\partial_{\tau_{r3}}a_0-\eta c_0)\}+\varepsilon^{-1}\{-\nabla_{\mathbf{x}}\cdot\mathbf{D}\nabla_{\mathbf{y}}a_0-\nabla_{\mathbf{y}}\cdot\mathbf{D}(\nabla_{\mathbf{y}}a_1+\nabla_{\mathbf{x}}a_0)\\&\quad+\varepsilon^{1-\alpha}[\partial_{\tau_a}a_0+\varepsilon^{\alpha+\beta}\partial_{\tau_{r1}}a_0+\nabla_{\mathbf{x}}\cdot(a_0\mathbf{v}_0)+\nabla_{\mathbf{y}}\cdot(a_1\mathbf{v}_0+a_0\mathbf{v}_1)]\\&\quad+\varepsilon^{2+\gamma}[\partial_{\tau_{r2}}a_1+a_0b_1+a_1b_0]+\varepsilon^{2+\delta}[\partial_{\tau_{r3}}a_1-\eta c_1]\}\\&\quad+\varepsilon^{0}\{\partial_t a_0-\nabla_{\mathbf{x}}\cdot\mathbf{D}(\nabla_{\mathbf{x}}a_0+\nabla_{\mathbf{y}}a_1)-\nabla_{\mathbf{y}}\cdot\mathbf{D}(\nabla_{\mathbf{x}}a_1+\nabla_{\mathbf{y}}a_2)\\&\quad+\varepsilon^{1-\alpha}[\partial_{\tau_a}a_1+\varepsilon^{\alpha+\beta}\partial_{\tau_{r1}}a_1+\nabla_{\mathbf{x}}\cdot(a_1\mathbf{v}_0+a_0\mathbf{v}_1)\\&\quad+\nabla_{\mathbf{y}}\cdot(a_1\mathbf{v}_1+a_0\mathbf{v}_2+a_2\mathbf{v}_0)]+\varepsilon^{2+\gamma}[\partial_{\tau_{r2}}a_2+a_0b_2+b_0a_2+a_1b_1]\\&\quad+\varepsilon^{2+\delta}[\partial_{\tau_{r3}}a_2-\eta c_2]\}=\mathcal{O}(\varepsilon),\quad \mathbf{y}\in\mathcal{B},\end{aligned} \tag{A.5}$$

subject to the boundary condition

$$\begin{aligned}&\varepsilon^{-1}\left[\mathbf{n}\cdot\mathbf{D}\nabla_{\mathbf{y}}a_0\right]+\varepsilon^{0}\left[\mathbf{n}\cdot\mathbf{D}(\nabla_{\mathbf{x}}a_0+\nabla_{\mathbf{y}}a_1)\right]\\&\quad+\varepsilon\left[\mathbf{n}\cdot\mathbf{D}(\nabla_{\mathbf{x}}a_1+\nabla_{\mathbf{y}}a_2)\right]=\mathcal{O}(\varepsilon^2),\quad \mathbf{y}\in\Gamma.\end{aligned} \tag{A.6}$$

The equation for c reads as follows

$$\begin{aligned}&\varepsilon^{-2}\{\nabla_{\mathbf{y}}\cdot(-\mathbf{D}\nabla_{\mathbf{y}}c_0+\varepsilon^{1-\alpha}c_0\mathbf{v}_0)+\varepsilon^{2+\gamma}(\partial_{\tau_{r2}}c_0-\eta^{-1}a_0b_0)\\&\quad+\varepsilon^{2+\delta}(\partial_{\tau_{r3}}c_0+c_0)\}+\varepsilon^{-1}\{-\nabla_{\mathbf{x}}\cdot\mathbf{D}\nabla_{\mathbf{y}}c_0-\nabla_{\mathbf{y}}\cdot\mathbf{D}(\nabla_{\mathbf{y}}c_1+\nabla_{\mathbf{x}}c_0)\\&\quad+\varepsilon^{1-\alpha}[\partial_{\tau_a}c_0+\varepsilon^{\alpha+\beta}\partial_{\tau_{r1}}c_0+\nabla_{\mathbf{x}}\cdot(c_0\mathbf{v}_0)+\nabla_{\mathbf{y}}\cdot(c_1\mathbf{v}_0+c_0\mathbf{v}_1)]\\&\quad+\varepsilon^{2+\gamma}[\partial_{\tau_{r2}}c_1-\eta^{-1}(a_0b_1-a_1b_0)]+\varepsilon^{2+\delta}[\partial_{\tau_{r3}}c_1+c_1]\}\\&\quad+\varepsilon^{0}\{\partial_t c_0-\nabla_{\mathbf{x}}\cdot\mathbf{D}(\nabla_{\mathbf{x}}c_0+\nabla_{\mathbf{y}}c_1)-\nabla_{\mathbf{y}}\cdot\mathbf{D}(\nabla_{\mathbf{x}}c_1+\nabla_{\mathbf{y}}c_2)\\&\quad+\varepsilon^{1-\alpha}[\partial_{\tau_a}c_1+\varepsilon^{\alpha+\beta}\partial_{\tau_{r1}}c_1+\nabla_{\mathbf{x}}\cdot(c_1\mathbf{v}_0+c_0\mathbf{v}_1)\\&\quad+\nabla_{\mathbf{y}}\cdot(c_1\mathbf{v}_1+c_0\mathbf{v}_2+c_2\mathbf{v}_0)]+\varepsilon^{2+\gamma}[\partial_{\tau_{r2}}c_2-\eta^{-1}(a_0b_2-b_0a_2-a_1b_1)]\\&\quad+\varepsilon^{2+\delta}[\partial_{\tau_{r3}}c_2+c_2]\}=\mathcal{O}(\varepsilon),\quad \mathbf{y}\in\mathcal{B},\end{aligned} \tag{A.7}$$

subject to

$$\begin{aligned}&\varepsilon^{-1}(-\mathbf{n}\cdot\mathbf{D}\nabla_{\mathbf{y}}c_0)+\varepsilon^{0}[-\mathbf{n}\cdot\mathbf{D}(\nabla_{\mathbf{x}}c_0+\nabla_{\mathbf{y}}c_1)-\varepsilon^{\beta}(c_0^n-1)]\\&\quad+\varepsilon[-\mathbf{n}\cdot\mathbf{D}(\nabla_{\mathbf{x}}c_1+\nabla_{\mathbf{y}}c_2)-\varepsilon^{\beta}nc_0^{n-1}c_1]=\mathcal{O}(\varepsilon^2),\quad \mathbf{y}\in\Gamma.\end{aligned} \tag{A.8}$$

A.1. Terms of order $\mathcal{O}(\varepsilon^{-2})$

Collecting the leading-order terms in (A.5) and (A.6), we obtain

$$\begin{aligned}&\nabla_{\mathbf{y}}\cdot(-\mathbf{D}\nabla_{\mathbf{y}}a_0+\varepsilon^{1-\alpha}a_0\mathbf{v}_0)+\varepsilon^{2+\gamma}(\partial_{\tau_{r2}}a_0+a_0b_0)\\&\quad+\varepsilon^{2+\delta}(\partial_{\tau_{r3}}a_0-\eta c_0)=0,\quad \mathbf{y}\in\mathcal{B},\end{aligned} \tag{A.9}$$

subject to

$$\mathbf{n}\cdot\mathbf{D}\nabla_{\mathbf{y}}a_0=0,\quad \mathbf{y}\in\Gamma. \tag{A.10}$$

Since (A.9) and (A.10) are homogeneous, the solution does not depend on $\mathbf{y}$, i.e. $a_0=a_0(\mathbf{x},t,\tau_a,\tau_{r1},\tau_{r2},\tau_{r3})$. The same result applies to b_0 and c_0.

A.2. Terms of order $\mathcal{O}(\varepsilon^{-1})$

Since $\nabla_{\mathbf{y}}a_0=\mathbf{0}$, collecting terms of $\mathcal{O}(\varepsilon^{-1})$ leads to

$$\begin{aligned}&-\nabla_{\mathbf{y}}\cdot\mathbf{D}(\nabla_{\mathbf{y}}a_1+\nabla_{\mathbf{x}}a_0)+\varepsilon^{1-\alpha}[\partial_{\tau_a}a_0+\varepsilon^{\alpha+\beta}\partial_{\tau_{r1}}a_0+\nabla_{\mathbf{x}}\cdot(a_0\mathbf{v}_0)\\&+\nabla_{\mathbf{y}}\cdot(a_1\mathbf{v}_0+a_0\mathbf{v}_1)]+\varepsilon^{2+\gamma}[\partial_{\tau_{r2}}a_1+(a_0b_1+a_1b_0)]\\&+\varepsilon^{2+\delta}[\partial_{\tau_{r3}}a_1-\eta c_1]=0,\quad \mathbf{y}\in\mathcal{B},\end{aligned} \tag{A.11}$$

subject to the boundary conditions

$$-\mathbf{n}\cdot\mathbf{D}(\nabla_{\mathbf{x}}a_0+\nabla_{\mathbf{y}}a_1)=0,\quad \mathbf{y}\in\Gamma. \tag{A.12}$$

Boundary conditions for c read

$$-\mathbf{n}\cdot\mathbf{D}(\nabla_{\mathbf{x}}c_0+\nabla_{\mathbf{y}}c_1)=\varepsilon^{\beta}(c_0^n-1),\quad \mathbf{y}\in\Gamma. \tag{A.13}$$

Integrating (A.11) over $\mathcal{B}$, while accounting for (A.12) and the no-slip boundary condition, gives

$$\begin{aligned}\varepsilon^{1-\alpha}\partial_{\tau_a}a_0+\varepsilon^{1+\beta}\partial_{\tau_{r1}}a_0=&-\varepsilon^{1-\alpha}\nabla_{\mathbf{x}}\cdot\left(a_0\langle\mathbf{v}_0\rangle_{\mathcal{B}}\right)\\&-\varepsilon^{2+\gamma}\left[\partial_{\tau_{r2}}\langle a_1\rangle_{\mathcal{B}}+\left(a_0\langle b_1\rangle_{\mathcal{B}}+b_0\langle a_1\rangle_{\mathcal{B}}\right)\right]\\&-\varepsilon^{2+\delta}\left[\partial_{\tau_{r3}}\langle a_1\rangle_{\mathcal{B}}-\eta\langle c_1\rangle_{\mathcal{B}}\right].\end{aligned} \tag{A.14}$$

Combining (A.11) and (A.14), while accounting for $\nabla_{\mathbf{y}}\cdot\mathbf{v}_0=0,\nabla_{\mathbf{x}}\cdot\langle\mathbf{v}_0\rangle_{\mathcal{B}}=0,\nabla_{\mathbf{y}}\cdot\mathbf{v}_1+\nabla_{\mathbf{x}}\cdot\mathbf{v}_0=0$, and $\nabla_{\mathbf{y}}a_0=\mathbf{0}$, leads to

$$\begin{aligned}&-\nabla_{\mathbf{y}}\cdot\mathbf{D}(\nabla_{\mathbf{y}}a_1+\nabla_{\mathbf{x}}a_0)+\varepsilon^{1-\alpha}[(\mathbf{v}_0-\langle\mathbf{v}_0\rangle_{\mathcal{B}})\cdot\nabla_{\mathbf{x}}a_0+\mathbf{v}_0\cdot\nabla_{\mathbf{y}}a_1]\\&\quad+\varepsilon^{2+\gamma}[\partial_{\tau_{r2}}(a_1-\langle a_1\rangle_{\mathcal{B}})+a_0(b_1-\langle b_1\rangle_{\mathcal{B}})+b_0(a_1-\langle a_1\rangle_{\mathcal{B}})]\\&\quad+\varepsilon^{2+\delta}\left[\partial_{\tau_{r3}}(a_1-\langle a_1\rangle_{\mathcal{B}})-\eta(c_1-\langle c_1\rangle_{\mathcal{B}})\right]=0,\quad \mathbf{y}\in\mathcal{B},\end{aligned} \tag{A.15}$$

subject to

$$-\mathbf{n}\cdot\mathbf{D}(\nabla_{\mathbf{x}}a_0+\nabla_{\mathbf{y}}a_1)=0,\quad \mathbf{y}\in\Gamma. \tag{A.16}$$

Similarly, the boundary value problem for species C reads as follows

$$\begin{aligned}&-\nabla_{\mathbf{y}}\cdot\mathbf{D}(\nabla_{\mathbf{y}}c_1+\nabla_{\mathbf{x}}c_0)+\varepsilon^{1-\alpha}[(\mathbf{v}_0-\langle\mathbf{v}_0\rangle_{\mathcal{B}})\cdot\nabla_{\mathbf{x}}c_0+\mathbf{v}_0\cdot\nabla_{\mathbf{y}}c_1\\&\quad-\varepsilon^{\alpha+\beta-1}\mathcal{K}^{\star}(c_0^n-1)]+\varepsilon^{2+\gamma}\{\partial_{\tau_{r2}}(c_1-\langle c_1\rangle_{\mathcal{B}})-\eta^{-1}[a_0(b_1+\langle b_1\rangle_{\mathcal{B}})\\&\quad+b_0(a_1-\langle a_1\rangle_{\mathcal{B}})]\}+\varepsilon^{2+\delta}[\partial_{\tau_{r3}}(c_1-\langle c_1\rangle_{\mathcal{B}})+(c_1-\langle c_1\rangle_{\mathcal{B}})]=0,\quad \mathbf{y}\in\mathcal{B},\end{aligned} \tag{A.17}$$

where $\mathcal{K}^{\star}=|\Gamma||\mathcal{B}|^{-1}$, and is subject to the non-homogeneous boundary condition

$$-\mathbf{n}\cdot\mathbf{D}(\nabla_{\mathbf{x}}c_0+\nabla_{\mathbf{y}}c_1)=\varepsilon^{\beta}(c_0^n-1),\quad \mathbf{y}\in\Gamma. \tag{A.18}$$

Eqs. (A.15), (A.16) and (A.17), (A.18) represent a boundary value problem for a_1 (or b_1) and c_1, respectively. We look for a solution in the following form

$$\psi_1(\mathbf{x},\mathbf{y},t,\tau_a,\boldsymbol{\tau}_r)=\boldsymbol{\chi}_{\psi}(\mathbf{y})\cdot\nabla_{\mathbf{x}}\psi_0(\mathbf{x},t,\tau_a,\boldsymbol{\tau}_r)+\overline{\psi}_1(\mathbf{x},t,\tau_a,\boldsymbol{\tau}_r),\quad \psi=\{a,b,c\}, \tag{A.19}$$

where the dependence upon $\mathbf{y}$ is isolated in the Y-periodic closure variable $\boldsymbol{\chi}_{\psi}$, with zero mean $\langle\boldsymbol{\chi}_{\psi}\rangle$. Inserting (A.19) in (A.15), (A.16), (A.17) and (A.18), we obtain

$$\begin{aligned}&[-\nabla_{\mathbf{y}}\cdot\mathbf{D}(\nabla_{\mathbf{y}}\boldsymbol{\chi}_a+\mathbf{I})+\varepsilon^{1-\alpha}\mathbf{v}_0\cdot\nabla_{\mathbf{y}}\boldsymbol{\chi}_a]\cdot\nabla_{\mathbf{x}}a_0\\&\quad+\varepsilon^{2+\gamma}\left[\partial_{\tau_{r2}}(\boldsymbol{\chi}_a\cdot\nabla_{\mathbf{x}}a_0)+a_0\boldsymbol{\chi}_b\cdot\nabla_{\mathbf{x}}b_0+b_0\boldsymbol{\chi}_a\cdot\nabla_{\mathbf{x}}a_0\right]\\&\quad+\varepsilon^{2+\delta}[\partial_{\tau_{r3}}(\boldsymbol{\chi}_a\cdot\nabla_{\mathbf{x}}a_0)-\eta\boldsymbol{\chi}_c\cdot\nabla_{\mathbf{x}}c_0]\\&\quad=\varepsilon^{1-\alpha}\left(\langle\mathbf{v}_0\rangle_{\mathcal{B}}-\mathbf{v}_0\right)\cdot\nabla_{\mathbf{x}}a_0,\quad \mathbf{y}\in\mathcal{B},\end{aligned} \tag{A.20}$$

subject to

$$-\mathbf{n}\cdot\mathbf{D}(\nabla_{\mathbf{y}}\boldsymbol{\chi}_a+\mathbf{I})=0,\quad \mathbf{y}\in\Gamma, \tag{A.21}$$

if $\nabla_{\mathbf{x}}a_0\neq\mathbf{0}$, and

$$\begin{aligned}&[-\nabla_{\mathbf{y}}\cdot\mathbf{D}(\nabla_{\mathbf{y}}\boldsymbol{\chi}_c+\mathbf{I})+\varepsilon^{1-\alpha}\mathbf{v}_0\cdot\nabla_{\mathbf{y}}\boldsymbol{\chi}_c]\cdot\nabla_{\mathbf{x}}c_0\\&\quad+\varepsilon^{2+\gamma}[\partial_{\tau_{r2}}(\boldsymbol{\chi}_c\cdot\nabla_{\mathbf{x}}c_0)-\eta^{-1}(a_0\boldsymbol{\chi}_b\cdot\nabla_{\mathbf{x}}b_0+b_0\boldsymbol{\chi}_a\cdot\nabla_{\mathbf{x}}a_0)]\\&\quad+\varepsilon^{2+\delta}[\partial_{\tau_{r3}}(\boldsymbol{\chi}_c\cdot\nabla_{\mathbf{x}}c_0)+\boldsymbol{\chi}_c\cdot\nabla_{\mathbf{x}}c_0]-\varepsilon^{\beta}\mathcal{K}^{\star}(c_0^n-1)\\&\quad=\varepsilon^{1-\alpha}(\langle\mathbf{v}_0\rangle_{\mathcal{B}}-\mathbf{v}_0)\cdot\nabla_{\mathbf{x}}c_0,\quad \mathbf{y}\in\mathcal{B},\end{aligned} \tag{A.22}$$

subject to

$$-\left[\mathbf{n}\cdot\mathbf{D}(\nabla_{\mathbf{y}}\boldsymbol{\chi}_c+\mathbf{I})\right]\cdot\nabla_{\mathbf{x}}c_0=\varepsilon^{\beta}(c_0^n-1),\quad \mathbf{y}\in\Gamma, \tag{A.23}$$

respectively. The boundary value problems for the closure variables $\boldsymbol{\chi}_{\psi},\psi=\{a,b,c\}$ are generally fully coupled to the macroscale through ψ_0 and its gradients. In order to ensure that the closure problem is fully decoupled from its continuum-scale counterpart and $\boldsymbol{\chi}_{\psi}$ is function of $\mathbf{y}$ only, consistently with (A.19), all the terms

in (A.20)–(A.23) containing macroscopic quantities must be negligible as $\varepsilon \ll 1$. We first observe that no additional constraints are required to decouple (A.20)-(A.21) from the macroscale problem, if $\boldsymbol{\chi}_c$ is function of $\mathbf{y}$ only. We start with the boundary value problem (A.22)-(A.23) for $\boldsymbol{\chi}_c$. The right-hand side in (A.23) is negligible compared to the left-hand side if $\beta > 0$ (constraint 4). Additionally, for the terms of order $\varepsilon^{\beta}, \varepsilon^{2+\gamma}$ and $\varepsilon^{2+\delta}$ to be negligible relative to the smallest term in (A.22), β, γ and δ must satisfy the following constraints: $\beta > \max\{0, 1-\alpha\}, 2+\gamma > \max\{0, 1-\alpha\}$, and $2+\delta > \max\{0, 1-\alpha\}$, respectively. Since $\alpha < 2$ (constraint 3), then $\beta > 0, \gamma > -2$ (constraint 5) and $\delta > -2$ (constraint 6) if $1 < \alpha < 2$, and $\beta > 1-\alpha$ (constraint 7), $\gamma > -1-\alpha$ (constraint 8) and $\delta > -1-\alpha$ (constraint 9) if $\alpha < 1$.

A.3. Terms of order $\mathcal{O}(\varepsilon^0)$

Collecting terms of order ε^0 in (A.5), leads to

$$\begin{aligned}&\partial_t a_0 - \nabla_{\mathbf{x}} \cdot \mathbf{D}(\nabla_{\mathbf{x}} a_0 + \nabla_{\mathbf{y}} a_1) - \nabla_{\mathbf{y}} \cdot \mathbf{D}(\nabla_{\mathbf{x}} a_1 + \nabla_{\mathbf{y}} a_2)\\ &\quad + \varepsilon^{1-\alpha}[\partial_{\tau_a} a_1 + \varepsilon^{\alpha+\beta}\partial_{\tau_{r1}} a_1 + \nabla_{\mathbf{x}} \cdot (a_1 \mathbf{v}_0 + a_0 \mathbf{v}_1)\\ &\quad + \nabla_{\mathbf{y}} \cdot (a_1 \mathbf{v}_1 + a_0 \mathbf{v}_2 + a_2 \mathbf{v}_0)] + \varepsilon^{2+\gamma}[\partial_{\tau_{r2}} a_2 + a_0 b_2 + b_0 a_2 + a_1 b_1]\\ &\quad + \varepsilon^{2+\delta}[\partial_{\tau_{r3}} a_2 - \eta c_2] = 0, \quad \mathbf{y} \in \mathcal{B}, \end{aligned} \tag{A.24}$$

subject to

$$-\mathbf{n} \cdot \mathbf{D}(\nabla_{\mathbf{x}} a_1 + \nabla_{\mathbf{y}} a_2) = 0, \quad \mathbf{y} \in \Gamma. \tag{A.25}$$

Integration of (A.24) over $\mathcal{B}$ with respect to $\mathbf{y}$ while accounting for (A.25), (A.19) and periodicity, leads to

$$\begin{aligned}&\partial_t \langle a_0 \rangle_{\mathcal{B}} - \nabla_{\mathbf{x}} \cdot \langle \mathbf{D}(\mathbf{I} + \nabla_{\mathbf{y}} \boldsymbol{\chi}_a) \rangle_{\mathcal{B}} \nabla_{\mathbf{x}} a_0\\ &\quad + \varepsilon^{1-\alpha}[\partial_{\tau_a} \langle a_1 \rangle_{\mathcal{B}} + \varepsilon^{\alpha+\beta}\partial_{\tau_{r1}} \langle a_1 \rangle_{\mathcal{B}} + \nabla_{\mathbf{x}} \cdot (\langle a_1 \mathbf{v}_0 \rangle_{\mathcal{B}} + a_0 \langle \mathbf{v}_1 \rangle_{\mathcal{B}})]\\ &\quad + \varepsilon^{2+\gamma}[\partial_{\tau_{r2}} \langle a_2 \rangle_{\mathcal{B}} + a_0 \langle b_2 \rangle_{\mathcal{B}} + b_0 \langle a_2 \rangle_{\mathcal{B}} + \langle a_1 b_1 \rangle_{\mathcal{B}}]\\ &\quad + \varepsilon^{2+\delta}[\partial_{\tau_{r3}} \langle a_2 \rangle_{\mathcal{B}} - \eta \langle c_2 \rangle_{\mathcal{B}}] = 0. \end{aligned} \tag{A.26}$$

We insert (A.19) in (A.26) while accounting for the relationships $\psi_0 = \langle \psi_0 \rangle_{\mathcal{B}}$ and $\mathbf{v}_0 = -\mathbf{k}(\mathbf{y}) \cdot \nabla_{\mathbf{x}} p_0$, and obtain

$$\begin{aligned}&\partial_t \langle a_0 \rangle_{\mathcal{B}} + \varepsilon^{1-\alpha}\partial_{\tau_a} \langle a_1 \rangle_{\mathcal{B}} + \varepsilon^{1+\beta}\partial_{\tau_{r1}} \langle a_1 \rangle_{\mathcal{B}} + \varepsilon^{2+\gamma}\partial_{\tau_{r2}} \langle a_2 \rangle_{\mathcal{B}}\\ &\quad + \varepsilon^{2+\delta}\partial_{\tau_{r3}} \langle a_2 \rangle_{\mathcal{B}} = \nabla_{\mathbf{x}} \cdot (\phi^{-1} \mathbf{D}^{\star} \nabla_{\mathbf{x}} \langle a_0 \rangle_{\mathcal{B}})\\ &\quad - \phi^{-1} \varepsilon^{1-\alpha} \nabla_{\mathbf{x}} \cdot (\langle a_0 \rangle_{\mathcal{B}} \langle \mathbf{v}_1 \rangle + \bar{a}_1 \langle \mathbf{v}_0 \rangle) - \varepsilon^{2+\gamma}(\langle a_0 \rangle_{\mathcal{B}} \langle b_2 \rangle_{\mathcal{B}}\\ &\quad + \langle b_0 \rangle_{\mathcal{B}} \langle a_2 \rangle_{\mathcal{B}} + \langle a_1 b_1 \rangle_{\mathcal{B}}) + \varepsilon^{2+\delta} \eta \langle c_2 \rangle_{\mathcal{B}}, \end{aligned} \tag{A.27}$$

where $\mathbf{D}^{\star} = \langle \mathbf{D}(\mathbf{I} + \nabla_{\mathbf{y}} \boldsymbol{\chi}_a) \rangle + \varepsilon^{1-\alpha} \langle \boldsymbol{\chi}_a \mathbf{k} \rangle \nabla_{\mathbf{x}} p_0$. Multiplying (A.27) by ε and adding it to (A.14) and to the integral of (A.9) over $\mathcal{B}$ gives

$$\begin{aligned}\varepsilon \partial_t \langle a \rangle_{\mathcal{B}} = {}& \varepsilon \nabla_{\mathbf{x}} \cdot (\phi^{-1} \mathbf{D}^{\star} \nabla_{\mathbf{x}} \langle a_0 \rangle_{\mathcal{B}}) - \varepsilon^{1-\alpha} \nabla_{\mathbf{x}} \cdot (\langle a_0 \rangle_{\mathcal{B}} \langle \mathbf{v}_0 \rangle_{\mathcal{B}}\\ &+ \varepsilon \langle a_0 \rangle_{\mathcal{B}} \langle \mathbf{v}_1 \rangle_{\mathcal{B}} + \varepsilon \bar{a}_1 \langle \mathbf{v}_0 \rangle_{\mathcal{B}}) - \varepsilon^{1+\gamma}[\langle a_0 \rangle_{\mathcal{B}} \langle b_0 \rangle_{\mathcal{B}}\\ &+ \varepsilon(\langle a_0 \rangle_{\mathcal{B}} \langle b_1 \rangle_{\mathcal{B}} + \langle b_0 \rangle_{\mathcal{B}} \langle a_1 \rangle_{\mathcal{B}}) + \varepsilon^2 \langle a_0 \rangle_{\mathcal{B}} \langle b_2 \rangle_{\mathcal{B}}\\ &+ \langle b_0 \rangle_{\mathcal{B}} \langle a_2 \rangle_{\mathcal{B}} + \langle a_1 b_1 \rangle_{\mathcal{B}})] + \varepsilon^{1+\delta} \eta (\langle c_0 \rangle_{\mathcal{B}} + \varepsilon \langle c_1 \rangle_{\mathcal{B}}\\ &+ \varepsilon^2 \langle c_2 \rangle_{\mathcal{B}}) + \mathcal{O}(\varepsilon^2), \end{aligned} \tag{A.28}$$

since $\langle \psi \rangle_{\mathcal{B}} = \langle \psi_{\varepsilon} \rangle_{\mathcal{B}} = \langle \psi_0 \rangle_{\mathcal{B}} + \varepsilon \langle \psi_1 \rangle_{\mathcal{B}} + \mathcal{O}(\varepsilon^2)$, and

$$\begin{aligned}\varepsilon \partial_t \langle a \rangle_{\mathcal{B}} = {}& \varepsilon \partial_t \langle a_0 \rangle_{\mathcal{B}} + \varepsilon^{1-\alpha} \partial_{\tau_a} \langle a_0 \rangle_{\mathcal{B}} + \varepsilon \mathrm{Da}_j \partial_{\tau_{\eta j}} \langle a_0 \rangle_{\mathcal{B}} + \varepsilon(\varepsilon \partial_t \langle a_1 \rangle_{\mathcal{B}}\\ &+ \varepsilon^{1-\alpha} \partial_{\tau_a} \langle a_1 \rangle_{\mathcal{B}} + \varepsilon \mathrm{Da}_j \partial_{\tau_{\eta j}} \langle a_1 \rangle_{\mathcal{B}}) + \mathcal{O}(\varepsilon^2) \end{aligned} \tag{A.29}$$

with $\mathrm{Da}_j, j = \{1, 2, 3\}$, defined in (19). Additionally, using (A.19), (18) and (15), it can be showed that $\bar{a}_1 = \langle a_1 \rangle_{\mathcal{B}}, \langle a \rangle_{\mathcal{B}} \langle \mathbf{v} \rangle_{\mathcal{B}} = \langle a_0 \rangle_{\mathcal{B}} \langle \mathbf{v}_0 \rangle_{\mathcal{B}} + \varepsilon \langle a_0 \rangle_{\mathcal{B}} \langle \mathbf{v}_1 \rangle_{\mathcal{B}} + \varepsilon \langle a_1 \rangle_{\mathcal{B}} \langle \mathbf{v}_0 \rangle_{\mathcal{B}} + \mathcal{O}(\varepsilon^2), \varepsilon \langle a \rangle_{\mathcal{B}} = \varepsilon \langle a_0 \rangle_{\mathcal{B}} + \mathcal{O}(\varepsilon^2)$ and $\langle a \rangle_{\mathcal{B}} \langle b \rangle_{\mathcal{B}} = \langle a_0 \rangle_{\mathcal{B}} \langle b_0 \rangle_{\mathcal{B}} + \varepsilon(\langle a_0 \rangle_{\mathcal{B}} \langle b_1 \rangle_{\mathcal{B}} + \langle b_0 \rangle_{\mathcal{B}} \langle a_1 \rangle_{\mathcal{B}}) + \mathcal{O}(\varepsilon^2)$. Finally, accounting for the previous equalities while retaining terms of order up to ε in (A.28), we obtain (22a). The latter describes pore-scale processes within errors of order ε^2.

Collecting terms of order ε^0 in (A.7) leads to

$$\begin{aligned}&\partial_t c_0 - \nabla_{\mathbf{x}} \cdot \mathbf{D}(\nabla_{\mathbf{x}} c_0 + \nabla_{\mathbf{y}} c_1) - \nabla_{\mathbf{y}} \cdot \mathbf{D}(\nabla_{\mathbf{x}} c_1 + \nabla_{\mathbf{y}} c_2)\\ &\quad + \varepsilon^{1-\alpha}[\partial_{\tau_a} c_1 + \varepsilon^{\alpha+\beta}\partial_{\tau_{r1}} c_1 + \nabla_{\mathbf{x}} \cdot (c_1 \mathbf{v}_0 + c_0 \mathbf{v}_1)\\ &\quad + \nabla_{\mathbf{y}} \cdot (c_1 \mathbf{v}_1 + c_0 \mathbf{v}_2 + c_2 \mathbf{v}_0)]\\ &\quad + \varepsilon^{2+\gamma}[\partial_{\tau_{r2}} c_2 - \eta^{-1}(a_0 b_2 + b_0 a_2 + a_1 b_1)]\\ &\quad + \varepsilon^{2+\delta}[\partial_{\tau_{r3}} c_2 + c_2] = 0, \quad \mathbf{y} \in \mathcal{B}, \end{aligned} \tag{A.30}$$

subject to

$$-\mathbf{n} \cdot \mathbf{D}(\nabla_{\mathbf{x}} c_1 + \nabla_{\mathbf{y}} c_2) = n \varepsilon^{\beta} c_0^{n-1} c_1, \quad \mathbf{y} \in \Gamma. \tag{A.31}$$

A similar procedure to that just presented allows one to derive (22c) for $\langle c \rangle_{\mathcal{B}} = \langle c_0 \rangle_{\mathcal{B}} + \varepsilon \langle c_1 \rangle_{\mathcal{B}} + \mathcal{O}(\varepsilon^2)$, while imposing the additional constraint $\langle \boldsymbol{\chi}_c \rangle_{\Gamma} = \langle \boldsymbol{\chi}_c \rangle_{\mathcal{B}}$. Eqs. (22a)–(22c) govern the dynamics of $\langle a \rangle_{\mathcal{B}}, \langle b \rangle_{\mathcal{B}}$ and $\langle c \rangle_{\mathcal{B}}$ up to ε^2.

Appendix B. Notation

a_{ε}	dimensionless pore-scale aqueous concentration of species A.
$\hat{a}_{\varepsilon}$	pore-scale aqueous concentration of species A, [mol L^{-3}].
$\langle a_{\varepsilon} \rangle$	average of a_{ε} over the unit cell Y.
$\langle a_{\varepsilon} \rangle_{\mathcal{B}}$	average of a_{ε} over the pore volume $\mathcal{B}$.
$\langle a_{\varepsilon} \rangle_{\Gamma}$	average of a_{ε} over the solid–liquid interface Γ.
b_{ε}	dimensionless aqueous concentration of species B.
$\hat{b}_{\varepsilon}$	pore-scale aqueous concentration of species B, [mol L^{-3}].
$\langle b_{\varepsilon} \rangle$	average of b_{ε} over the unit cell Y.
$\langle b_{\varepsilon} \rangle_{\mathcal{B}}$	average of b_{ε} over the pore volume $\mathcal{B}$.
$\langle b_{\varepsilon} \rangle_{\Gamma}$	average of b_{ε} over the solid–liquid interface Γ.
$\mathcal{B}$	pore space domain in the unit cell Y.
$\lvert\mathcal{B}\rvert$	volume of $\mathcal{B}$.
$\mathcal{B}^{\varepsilon}$	pore space domain in the porous medium Ω.
c_{ε}	dimensionless pore-scale aqueous concentration of species C.
$\hat{c}_{\varepsilon}$	pore-scale aqueous concentration of species C, [mol L^{-3}].
$\langle c_{\varepsilon} \rangle$	average of c_{ε} over the unit cell Y.
$\langle c_{\varepsilon} \rangle_{\mathcal{B}}$	average of c_{ε} over the pore volume $\mathcal{B}$.
$\langle c_{\varepsilon} \rangle_{\Gamma}$	average of c_{ε} over the solid–liquid interface Γ.
$\bar{c}$	$:= \sqrt[n]{k_d/k}$, threshold aqueous concentration of species C, [mol L^{-3}].
$\hat{c}^{\star}$	$:= \max\{\hat{a}_{\mathrm{in}}, \hat{b}_{\mathrm{in}}\}$, characteristic value of concentrations $\hat{a}$ and $\hat{b}$, [mol L^{-3}].
$\mathbf{D}$	dimensionless molecular diffusion coefficient defined by (7).
$\mathcal{D}$	$:= \mathcal{D}_a = \mathcal{D}_b = \mathcal{D}_c$, [$L^2T^{-1}$].
$\mathcal{D}_i$	$i = \{a, b, c\}$, molecular diffusion coefficients for species A, B and C, respectively, [L^2T^{-1}].
$\mathcal{D}_0$	characteristic value of $\mathcal{D}$, [L^2T^{-1}].
$\mathbf{D}^{\star}$	dimensionless dispersion tensor defined by (23).
Da_j	$:= \hat{t}_d/\hat{t}_{\eta j}, j = \{1, 2, 3\}$, Damköhler numbers defined by (9).
$\mathcal{G}$	solid matrix domain in the unit cell Y.
k	reaction rate of the forward heterogeneous reaction $C \to S$.
k_{ab}	reaction rate of the forward homogeneous reaction $A + B \to C$.
k_c	reaction rate of the backward homogeneous reaction $A + B \leftarrow C$.
k_d	reaction rate of the backward heterogeneous reaction $C \leftarrow S$.
$\mathbf{k}$	closure variable defined by (21).
$\mathbf{K}$	$:= \langle \mathbf{k}(\mathbf{y}) \rangle$, permeability tensor.
$\mathcal{K}^{\star}$	effective reaction rate constant defined by (23).
ℓ	characteristic length of the periodic unit cell $\hat{Y}$.
L	characteristic length of macroscopic porous medium domain Ω.
n	heterogeneous reaction order, [-].
$\hat{p}$	fluid dynamic pressure, [$ML^{-1}T^{-2}$].
Pe	Péclet number defined by (9).
R_p	$:= k\hat{c}_{\varepsilon}^{n}$, precipitation rate.

R_d $:= k_d$, dissolution rate.
t $:= \hat{t}/\hat{t}_a$, dimensionless time.
$\hat{t}_a$ advection timescale, [T].
$\hat{t}_d$ diffusion timescale, [T].
$\hat{t}_{rj}$ $j = \{1, 2, 3\}$, reaction timescales, [T].
U characteristic velocity associated to $\hat{\mathbf{v}}_\varepsilon$, [$\mathrm{TL}^{-1}$].
$\mathbf{v}_\varepsilon$ dimensionless pore-scale fluid velocity.
$\hat{\mathbf{v}}_\varepsilon$ pore-scale fluid velocity, [TL^{-1}].
$\mathbf{x}$ spatial coordinate of the pore space $\mathcal{B}_\varepsilon$.
$\mathbf{y}$ spatial coordinate of the unit cell Y.
Y spatially periodic unit cell.
$|Y|$ volume of the spatially periodic unit cell.
ε $:= \ell/L$, scale separation coefficient, [-].
η $:= \overline{c}/\hat{c}^\star$, normalization coefficient, [-].
ϕ unit cell porosity, [-].
Γ solid–liquid interface in the unit cell Y.
Γ^ε solid–liquid interface in the porous medium Ω.
ν fluid dynamic viscosity, [$\mathrm{ML}^{-1}\mathrm{T}^{-1}$].
$\boldsymbol{\chi}_\psi$ $\psi = \{a, b, c\}$, closure variable for the transport problem of species ψ.
Ω porous medium domain.
ψ_{in} $\psi = \{a, b, c\}$, initial dimensionless concentration for species ψ.

References

[1] Allaire G, Brizzi R, Mikelić A, Piatnitski A. Two-scale expansion with drift approach to the Taylor dispersion for reactive transport through porous media. Chem Eng Sci 2010;65:2292–300.
[2] Auriault JL, Adler PM. Taylor dispersion in porous media: analysis by multiple scale expansions. Adv Water Resour 1995;18(4):217–26.
[3] Battiato I. Self-similarity in coupled Brinkman/Navier–Stokes flows. J Fluid Mech 2012;699:94–114.
[4] Battiato I, Bandaru PR, Tartakovsky DM. Elastic response of carbon nanotube forests to aerodynamic stresses. Phys Rev Lett 2010;105(14):144504.
[5] Battiato I, Tartakovsky DM. Applicability regimes for macroscopic models of reactive transport in porous media. J Contam Hydrol 2011;120–121:18–26.
[6] Battiato I, Tartakovsky DM, Tartakovsky AM, Scheibe TD. On breakdown of macroscopic models of mixing-controlled heterogeneous reactions in porous media. Adv Water Resour 2009;32:1664–73.
[7] Battiato I, Tartakovsky DM, Tartakovsky AM, Scheibe TM. Hybrid models of reactive transport in porous and fractured media. Adv Water Resour 2011;34(9):1140–50.
[8] Bear J. Dynamics of fluids in porous media. Dover; 1988.
[9] Blunt MJ, Jackson MD, Piri M, Valvatne PH. Detailed physics, predictive capabilities and macroscopic consequences for pore-network models of multiphase flow. Adv Water Resour 2002;25:1069–89.
[10] Boso F, Bellin A, Dumbser M. Numerical simulations of solute transport in highly heterogeneous formations: A comparison of alternative numerical schemes. Adv Water Resour 2013;52:178–89.
[11] Brenner H. Transport processes in porous media. McGraw-Hill; 1987.
[12] Choi T-J, Maurya MR, Tartakovsky DM, Subramaniam S. Stochastic hybrid modeling of intracellular calcium dynamics. J Chem Phys 2010;133(16):166101.
[13] Darcy H. Les fontaines publiques de la ville de Dijon. Paris: Victor Dalmont; 1856.
[14] Dentz M, Borgne TL, Englert A, Bijeljic B. Mixing spreading and reaction in heterogeneous media: a brief review. J Contam Hydrol 2011;120–121(0):1–17.
[15] Golfier F, Wood BD, Orgogozo L, Quintard M, Buès M. Biofilms in porous media: development of macroscopic transport equations via volume averaging with closure for local mass equilibrium conditions. Adv Water Resour 2009;32(3):463–85.
[16] Gray WG, Miller CT. Thermodynamically constrained averaging theory approach for modeling flow and transport phenomena in porous medium systems: 7. single-phase megascale flow models. Adv Water Resour 2009;32(8):1121–42.
[17] Herrera PA, Massabó M, Beckie RD. A meshless method to simulate solute transport in heterogeneous porous media. Adv Water Resour 2009;32(3):413–29.
[18] Higgins ER, Goel P, Puglisi JL, Bers DM, Cannell M, Sneyd J. Modelling calcium microdomains using homogenisation. J Theor Biol 2007;247(4):623–44.
[19] Hornung U. Homogenization and porous media. New York: Springer; 1997.
[20] Knabner P, Duijn CJV, Hengst S. An analysis of crystal dissolution fronts in flows through porous media. Part 1: compatible boundary conditions. Adv Water Resour 1995;18(3):171–85.
[21] Li L, Steefel CI, Yang L. Scale dependence of mineral dissolution rates within single pores and fractures. Geochim Cosmochim Ac 2008;72(2):360–77.
[22] Meile C, Tuncay K. Scale dependence of reaction rates in porous media. Adv Water Resour 2006;29:62–71.
[23] Mikelic A, Devigne V, Van Duijn CJ. Rigorous upscaling of the reactive flow through a pore, under dominant Péclet and Damköhler numbers. SIAM J Math Anal 2006;38(4):1262–87.
[24] Molins S, Trebotich D, Steefel CI, Shen CP, An investigation of the effect of pore scale flow on average geochemical reaction rates using direct numerical simulation, Water Resour Res, vol. 48 (W03527).
[25] Morse JW, Arvidson RS. The dissolution kinetics of major sedimentary carbonate minerals. Earth Sci Rev 2002;58:51–84.
[26] Neuman SP, Tartakovsky DM. Perspective on theories of anomalous transport in heterogeneous media. Adv Water Resour 2009;32(5):670–80.
[27] Pacala S, Socolow R. Stabilization wedges: solving the climate problem for the next 50 years with current technologies. Science 2004;305(5686):968–72.
[28] Peter MA. Analysis homogenization coupled reaction–diffusion processes inducing an evolution of the microstructure: analysis and homogenization. Nonlinear Anal : Theory Methods Appl 2009;70(2):806–21.
[29] Tartakovsky AM, Meakin P, Scheibe T. Simulations of reactive transport and precipitation with smoothed particle hydrodynamics. J Comput Phys 2007;222(2):654–72.
[30] Tartakovsky AM, Redden G, Lichtner PC, Scheibe TD, Meakin P. Mixing-induced precipitation: experimental study and multi-scale numerical analysis. Water Resour Res 2008;44(W06S04):19.
[31] Tartakovsky AM, Tartakovsky DM, Scheibe TD, Meakin P. Hybrid simulations of reaction–diffusion systems in porous media. SIAM J Sci Comput 2007;30(6):2799–816.
[32] Tartakovsky AM, Tartakovsky GD, Scheibe TD. Effects of incomplete mixing on multicomponent reactive transport. Adv Water Resour 2009;32(11):1674–9.
[33] Van Leemput P, Vandekerckhove C, Vanroose W, Roose D. Accuracy of hybrid lattice boltzmann/finite difference schemes for reaction-diffusion systems. Multiscale Model Simul 2007;6(3):838–57.
[34] van Noorden TL, Pop IS. A Stefan problem modelling crystal dissolution and precipitation. IMA J Appl Math 2008;73(2):393–411.
[35] Whitaker S. Levels of simplification: the use of assumptions, restrictions, and constraints in engineering analysis. Chem Eng Educ 1988;22:104–8.
[36] Whitaker S. The method of volume averaging. Kluwer Academic Publishers.; 1999.
[37] Willingham TW, Werth CJ, Valocchi AJ. Evaluation of the effects of porous media structure on mixing-controlled reactions using pore-scale modeling and micromodel experiments. Environ Sci Technol 2008;42(9):3185–93.
[38] Wood BD, Radakovich K, Golfier F. Effective reaction at a fluid-solid interface: applications to biotransformation in porous media. Adv Water Resour 2007;30:1630–47.